

# We are IntechOpen, the world's leading publisher of Open Access books Built by scientists, for scientists

5,800

Open access books available

142,000

International authors and editors

180M

Downloads

Our authors are among the

154

Countries delivered to

TOP 1%

most cited scientists

12.2%

Contributors from top 500 universities



WEB OF SCIENCE™

Selection of our books indexed in the Book Citation Index  
in Web of Science™ Core Collection (BKCI)

Interested in publishing with us?  
Contact [book.department@intechopen.com](mailto:book.department@intechopen.com)

Numbers displayed above are based on latest data collected.  
For more information visit [www.intechopen.com](http://www.intechopen.com)



# Recent Developments in the Crystallization of PLLA-Based Blends, Block Copolymers, and Nanocomposites

*Amit Kumar Pandey and Shinichi Sakurai*

## Abstract

Despite the extensive studies of poly(L-lactic acid) (PLLA), the crystallization of PLLA-based materials is still not completely understood. This chapter presents recent developments of crystallization of PLLA-based blends, block copolymers and nanocomposites. The first section of the chapter discusses the acceleration of PLLA crystallization by the inclusion of biobased (solid and liquid state) additives. It was found that the solid state additives work as a nucleating agent while the liquid-state additive works as a plasticizer. Both type of the additives can significantly enhance the crystallization of PLLA, as indicated by crystallization half-time ( $t_{0.5}$ ) values. Such composites are of great interest as they are 100% based on renewable resources. The second section talks about the enhanced formation of stereocomplex (SC) crystals in the PLLA/PDLA (50/50) blends by adding 1% SFN. It was found that the loading of SFN enhances the formation of SC crystals and it suppresses the formation of HC (homocrystal). The third section deals with confined crystallization of poly(ethylene glycol) (PEG) in a PLLA/PEG blend. The PLLA/PEG (50/50) blend specimen was heated up to 180.0°C and kept at this temperature for 5 min. Then, a two-step temperature-jump was conducted as 180.0°C → 127.0°C → 45.0°C. For this particular condition, it was found that PEG can crystallize only in the preformed spherulites of PLLA, as no crystallization of PEG was found in the matrix of the mixed PLLA/PEG amorphous phase. The last section describes the confined crystallization of PCL in the diblock and triblock copolymers of PLA-PCL. Furthermore, enantiomeric blends of PLLA-PCL and PDLA-PCL or PLLA-PCL-PLLA and PDLA-PCL-PDLA have been examined for the purpose of the improvement of the poor mechanical property of PLLA to which the SC formation of PLLA with PDLA components are relevant.

**Keywords:** Crystallization, poly(lactic acid), stereocomplex crystallization, poly(ethylene glycol), poly(caprolactone), biobased additives, improvement of crystallizability, X-ray scattering, crystalline block copolymer, crystalline polymer blend, confined crystallization

## 1. Introduction

Biobased polymers are gaining great popularity recently due to the increasing environmental concerns associated with conventional polymers. One such polymer

is poly(lactic acid) (PLA), which is obtained from 100% natural resources such as corn starch and sugar cane. PLA has a good advantage of mechanical strength and modulus (comparable to PET), however, it has slow crystallization rate, low elongation at break, and processing difficulties due to the low thermal stability which significantly restricts its practical applications. PLA exists in three optical isomeric forms poly(L-lactic acid) (PLLA), poly(D-lactic acid) (PDLA), and poly(D, L-lactic acid) (PDLLA). The PLLA and PDLA both can be partially crystallized with a melting temperature of 170–180 °C. However, a racemic blend (50% L and 50% D) gives an amorphous polymer. Generally, commercial PLA grades are comprised of L-lactic acid in majority with small amount of D moiety. The thermal and mechanical properties of PLLA are significantly affected by the presence of D units in PLLA [1].

The study of crystallization behavior of PLLA is very important to control its thermal, mechanical, and gas-barrier properties. The crystalline structure of PLLA has been studied by many researchers [2–5]. It has been reported that the crystallization of PLLA leads to several crystal forms ( $\alpha$ ,  $\alpha'$ ,  $\beta$ , and  $\gamma$ ). The  $\alpha$  form is the most stable polymorph which is developed from the melt or solution. The crystalline structure of PLLA  $\alpha$  form is pseudo-orthorhombic with dimensions of  $a = 1.0683$  nm,  $b = 0.617$  nm,  $c$  (chain axis) = 2.78 nm, where the molecules adopt a  $10_3$  helical conformation. Aleman et al. [6] proposed the space group of  $P2_12_12_1$  as the most plausible packing mode of  $10_3$  helices.

In this chapter, we review the recent developments [7–15] of crystallization of PLLA-based blends, block copolymers and nanocomposites. This chapter contains four sections. The first section deals with the enhancement in the crystallization of PLLA by adding biobased additives. Over the years, there have been several strategies employed by researchers to improve the crystallizability of PLLA [1, 16–19]. One of the most common and effective method is the addition of a nucleating agent. The nucleating agents are known to provide the sites for nucleation in polymers which results in the enhancement of overall crystallization process. Most of the nucleating agents reported for PLLA (talc, carbon nanotubes, graphene, clay) are inorganic materials that are non-biodegradable in nature [1, 20]. Recently, it is an emerging trend to utilize renewable resources for the improvement of crystallizability of PLLA. In this regard, we used solid-state biobased additives like silk fibroin nanodisc (SFN) and cellulose nanocrystal (CNC) with the aim of improving the crystallization of PLLA. The SFN is a biobased and environmentally benign material which was extracted from the waste of muga silk cocoons, which is composed of 83.8% poly(L-alanine) [21]. The CNC is also a biobased material which was extracted from the waste of marine green algae biomass residue (ABR). Further, we used liquid-state biobased additive, i.e., organic acid monoglyceride (OMG) for the sake of improvement of crystallizability of PLLA. The differential scanning calorimetry (DSC), polarizing optical microscopy (POM), synchrotron small-angle X-ray scattering (SAXS), and wide-angle X-ray scattering (WAXS) measurements were used for the study of crystallization of PLLA. It is worthy to mention here that the time-resolved SWAXS (simultaneous measurements of SAXS and WAXS) technique is one of the most promising technique to detect the initiation of nucleation and follow the change in the structure of growing crystals during the crystallization from the melt.

The second section talks about the stereocomplex crystallization of PLA. When PLLA (left-handed helix) and PDLA (right-handed helix) are mixed, the resultant mixture is known to form a complex so-called “stereocomplex (SC)”. The SC is known to improve the thermal stability of PLA [22, 23]. This is due to the approximately 50°C higher melting temperature of the SC crystals compared to the PLLA or PDLA homopolymer crystal (HC). While pure PLLA and PDLA crystallize in pseudo-orthorhombic form with a  $10_3$  helix conformation, the SC has a  $3_1$  helix form [24]. The crystalline structure of PLA stereocomplex is triclinic with dimension of  $a = b = 0.916$  nm,  $c$  (chain axis) = 0.87 nm,  $\alpha = \beta = 109.2^\circ$ , and  $\gamma = 109.8^\circ$ , in

which PLLA and PDLA chains are packed parallel taking  $3_1$  helical conformation [25]. The formation of SC is influenced by the molecular weights of PLLA and PDLA. It is very challenging to get SC crystals exclusively in the high molecular weight PLLA/PDLA blend due to the competing formation of SC and HC during the crystallization [26]. In view of this, we added 1% SFN in PLLA/PDLA (50/50) blend, aiming to enhance the SC crystallization.

The third section deals with the blend of PLLA and poly(ethylene glycol), PEG. PEG is a biocompatible polymer which is known for improving the toughness of PLLA [20, 27, 28]. The crystallization study of the PLLA/PEG blend is important from the aspect of the structural development, due to the fact that both the component (PLLA and PEG) are crystallizable having different  $T_g$  and  $T_m$ . Since PLLA and PEG are known to be miscible with each other, PLLA/PEG blend has attracted many researchers for the studies of structure control. Although there have been extensive research on the crystallization of PLLA part in the dual crystalline PLLA/PEG blend [28–32], the effect of PLLA spherulites on the PEG crystallization is not well-known. In this regard, we studied the effects of space confinement when the PEG crystallizes from the molten mixed amorphous phase sandwiched by the crystalline lamellae of the PLLA.

The final section of this chapter deals with the block copolymers of PLA (PLLA or PDLA) and poly( $\epsilon$ -caprolactone), PCL. PCL is a biodegradable polymer which is also known for improving the toughness of PLLA [28, 33]. Since it is known that PLA and PCL are immiscible, copolymerization is a better route in comparison with the blending to avoid the macro-phase separation. In view of this, we studied the crystallization behavior of dual crystalline PLLA-*b*-PCL, PDLA-*b*-PCL diblock copolymers by changing the block length of PLLA or PDLA, however, the block length of PCL was fixed. Furthermore, the blend of PLLA-*b*-PCL and PDLA-*b*-PCL is also studied for the study of formation of SC crystal by changing the block length of PLLA and PDLA components.

The PLLA samples were obtained from NatureWorks and the PDLA was obtained from Purac. The sample characteristics are summarized in **Table 1**. The specimens preparation method is mentioned in the respective section.

The DSC measurements for the isothermal crystallization were performed by DSC214 *Polyma* (NETZSCH, Germany). The specimens were first melted at 200°C (or 260°C) for 5 min and immediately cooled to  $T_{iso}$  with the cooling rate of 300°C/min, and kept isothermally until the completion of the crystallization process. POM observations were conducted by using a Nikon Eclipse Ci-POL polarizing optical microscope equipped with the Linkam THMS600 hot stage (Linkam Scientific, UK). The specimens were sandwiched between two coverslips. Next, the specimens were melted on the hot stage, then quickly cooled (cooling rate = 150°C/min) to the isothermal crystallization temperature, and then kept isothermally until the completion of the crystallization process. The POM images were taken under crossed polarizers with a 530 nm optical retardation plate inserted in the optical path. The time-resolved SWAXS measurements were carried out at the beamline BL-6A of Photon Factory at the KEK (High-Energy Accelerator Research Organization) in Tsukuba, Japan. The wavelength of the incident X-ray beam was 0.150 nm. The T-jump experiments were

Sample code	Optical purity	Number-average molecular weight ( $M_n$ )	$M_w/M_n$
PLLA 4032D (D1.4)	98.6%	$1.66 \times 10^5$	2.05
PLLA 2500HP (D0.5)	99.5%	$1.74 \times 10^5$	2.22
PDLA D130	> 99.5%	$1.41 \times 10^5$	2.03

**Table 1.**  
 Sample characterization.

conducted using a sample holder designed to allow for a quick T-jump (385°C/min). The details of the experimental set-up are reported elsewhere [7].

## 2. Improvement of PLLA crystallizability by biobased additives

### 2.1 Solid state additives (nucleation agents)

In this section, we report the effect of solid-state additives (SFN and CNC) on the isothermal crystallization of PLLA from the melt (200°C).

#### 2.1.1 Silk fibroin nanodisc (SFN)

The SFN used in this study was extracted from wastes of the muga silk (*Antheraea assama*) cocoon [21]. The crystalline portion (the  $\beta$  sheets) of the silk fibroin was isolated by using the acid-hydrolysis method. The obtained extract comprises 83.8% L-alanine, and the well-defined disc-like nano particles were obtained (see **Figure 1** for the chemical structure of poly(L-alanine)). Such morphology and dimensions have been reported as the average diameter and thickness of  $\sim 45$  nm and  $\sim 3$  nm, respectively [21]. The detailed information about the preparation of SFN can be found in Ref. [21]. PLLA/ SFN specimens were prepared by the solution-casting method, using dichloromethane (DCM) as a solvent [8]. The specimens are labeled as D1.4/SFN( $x$ ) or D0.5/SFN( $x$ ), where the numbers after D denote the % of D moiety in PLLA, and  $x$  stands for % of SFN inclusion.

POM observations were conducted to observe spherulites and to evaluate the growth rate of spherulites and the nucleation density as a function of time. The specimens were melted on the hot stage at 200°C for 3 min, then quickly cooled (cooling rate = 150°C/min) to the isothermal crystallization temperature ( $T_{iso}$ ) of 120°C, and then kept isothermally until the completion of the crystallization process. The representative images of the evolution of spherulites for the D1.4 neat and D1.4/SFN(1.0) specimens at 120°C as a function of time are shown in **Figure 2(a)** and **(b)**. First, negative spherulites were observed for both of the D1.4 neat and D1.4/SFN(1.0) specimens. As shown in **Figure 2(d)** the total number of spherulites increased  $\sim 4.7$  times (from 9 to 42). In addition, the induction period was shortened from 101 to 39 s. However, the growth rate of the spherulites was unchanged (5  $\mu\text{m}/\text{min}$ ) by the addition of SFN. These results clearly show that SFN can enhance nucleation of PLLA. SFN is considered to provide sites for easy formation of PLLA nuclei.

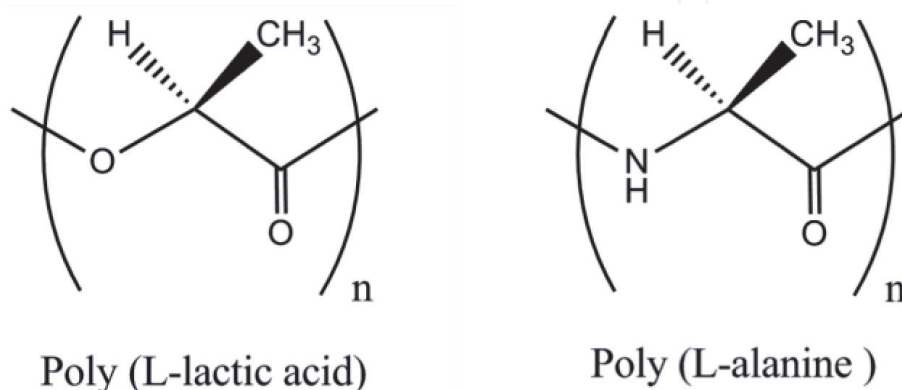


**Figure 1.**

Chemical structures of poly(L-lactic acid) and poly(L-alanine). L-alanine is the main component (83.8%) of the silk fibroin nanodisc.

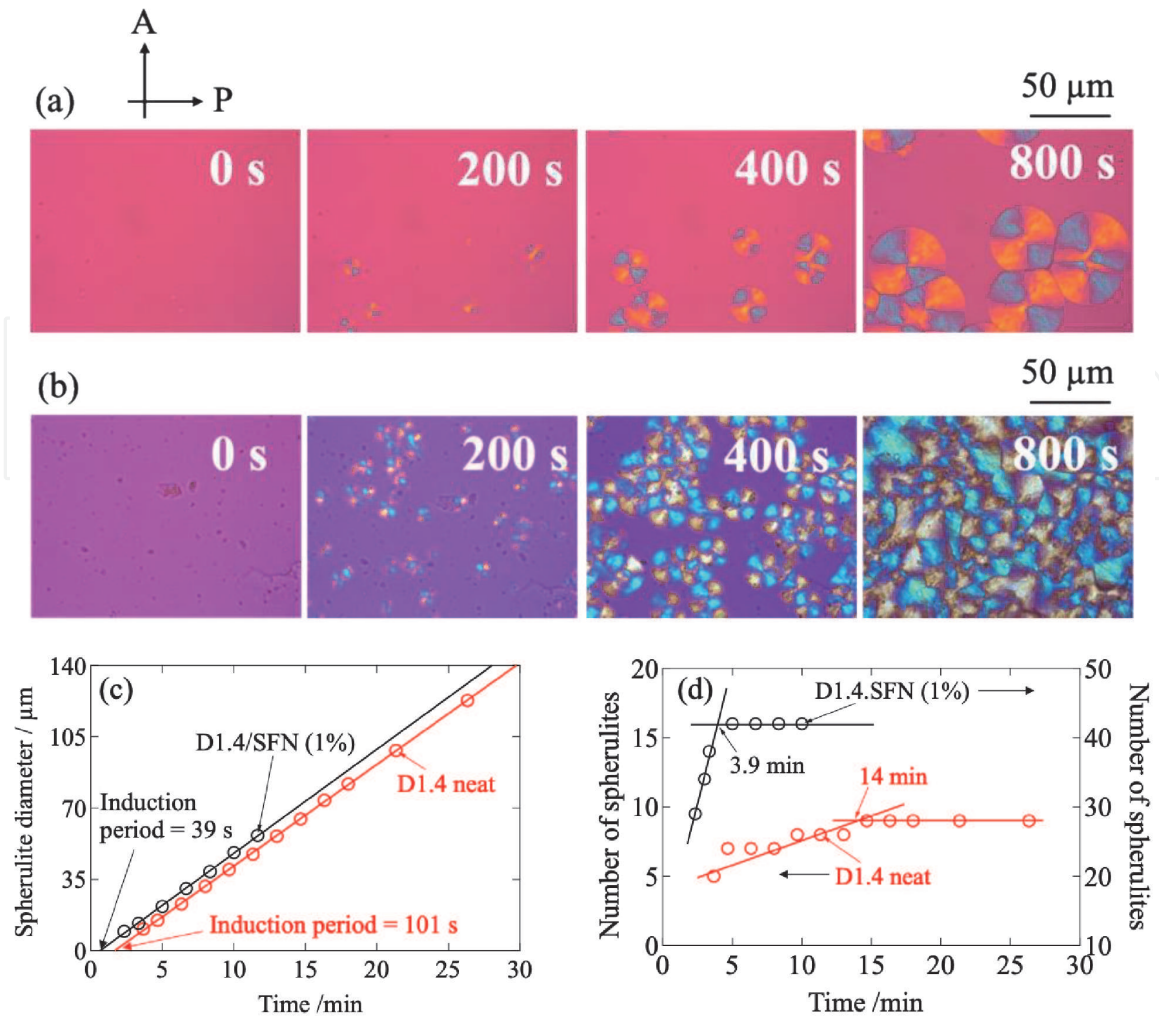


**Figure 2.** POM images as a function of time for isothermal crystallization at 120°C (a) D1.4 neat (b) D1.4/SFN(1.0) specimens. (c) Spherulite diameter and (d) the number of spherulites formed during the isothermal crystallization at 120°C (adapted from reference [8] with a permission).

**Figure 3** shows the DSC results of the isothermal crystallization of neat and 1% SFN included specimens at 110°C. the degree of PLLA crystallinity ( $\phi_{DSC}$ ) as evaluated based on the heat flow results using the following equation.

$$\phi_{DSC}(t) = \frac{\int_0^t H(t)dt}{\Delta H_m^o} \quad (1)$$

where  $t$  denotes time and  $\Delta H_m^o$  is the enthalpy of fusion for the 100% crystal of PLLA. The value of  $\Delta H_m^o$  is taken as 93 J/g, following reference [34]. **Figure 3(b)** clearly indicates that the induction period was reduced and the final degree of crystallinity was increased by the presence of SFN. Maximum achievable crystallinity was found in the case of D0.5/SFN(1.0).

The inverse of crystallization half-time ( $t_{0.5}$ ) can be used for the discussion of the crystallization rate, which is plotted as a function of the crystallization temperature in **Figure 4**. The graph shows a parabolic curve thereby producing maximum crystallization rate ( $1/t_{0.5,max}$ ). As shown in **Figure 4**, the overall crystallization growth rate was significantly increased by the inclusion of SFN, the maximum crystallization rate,  $1/t_{0.5,max}$ , was observed at 107.2°C. It should be noted that for both specimens D1.4 and D0.5, the crystallization rate showed the same tendency, as the most effective temperature is  $\sim 107^\circ\text{C}$ , although the  $T_m^O$  differs (The  $T_m^O$

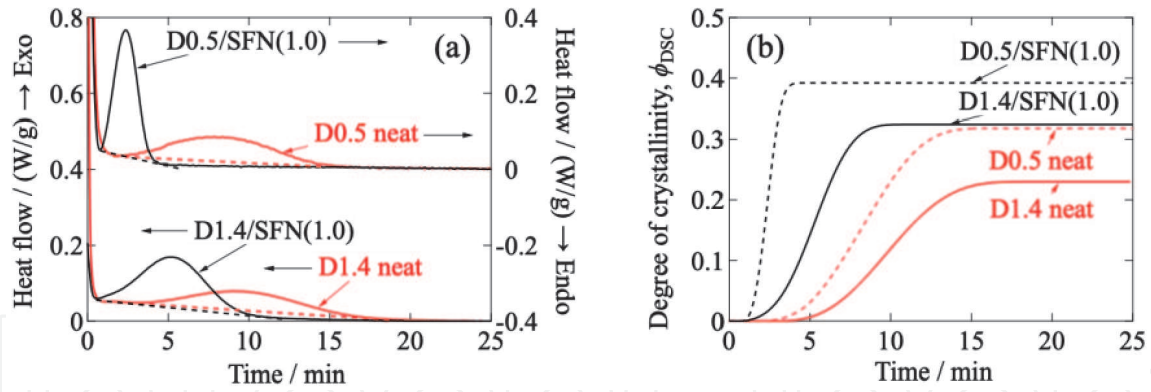


**Figure 3.** (a) Heat flow as a function of time during isothermal crystallization at 110°C and (b) degree of crystallinity ( $\phi_{DSC}$ ) as a function of time, which was evaluated based on the heat flow result (adapted from reference [8] with a permission).

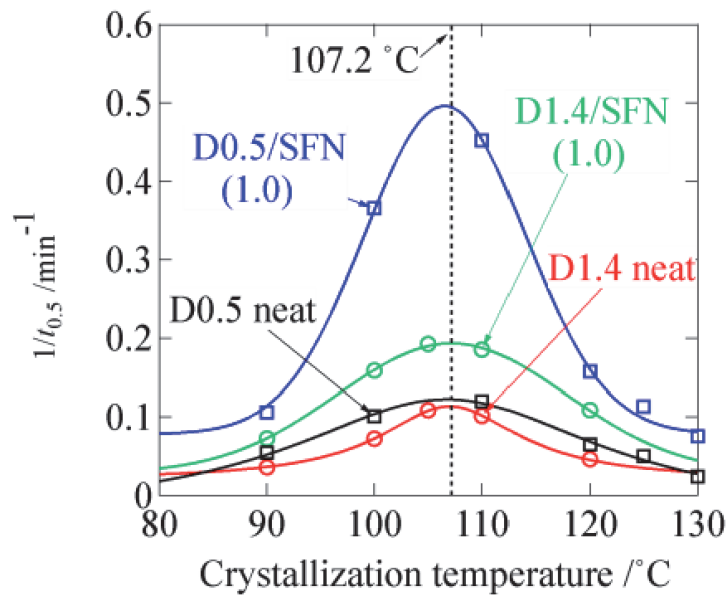


**Figure 4.** Inverse of crystallization half time as a function of crystallization temperature, calculated from DSC results (adapted from reference [8] with a permission).

values for the D1.4 neat and D0.5 neat specimens were 180.7°C and 193.3°C, respectively [8]). These results indicate that the PLLA crystallization is predominantly governed by the kinetic driving force ( $T - T_g$ ) rather than the thermodynamic driving force ( $T_m^O - T$ ). It is important to note here that the spherulite growth rate does not change in the presence of SFN (Figure 2), while  $1/t_{0.5}$  is increased. The reason for the enhancement of  $1/t_{0.5}$  can be attributed to the increased number of nuclei due to the addition of SFN (Figure 2). The enhanced nucleation of PLLA by SFN may be ascribed to the plausible formation of hydrogen bonding between the C=O group in PLLA and the N-H group of poly(L-alanine) (see the chemical structure in Figure 1).

Figure 5(a) and (b) show the time-resolved WAXS profiles for the D1.4 neat and D1.4/SFN(1.0) specimens as a function of time for isothermal crystallization at 110°C. Here, the magnitude of the scattering vector  $\mathbf{q}$  is defined as,  $|\mathbf{q}| = q = (4\pi/\lambda)$

$\sin(\theta/2)$  with  $\lambda$  and  $\theta$  being the wavelength of X-ray and the scattering angle, respectively. As shown in Figure 5(a) and (b), there is no crystalline peak initially, which shows the presence of 100% amorphous phase in the early stage. As time

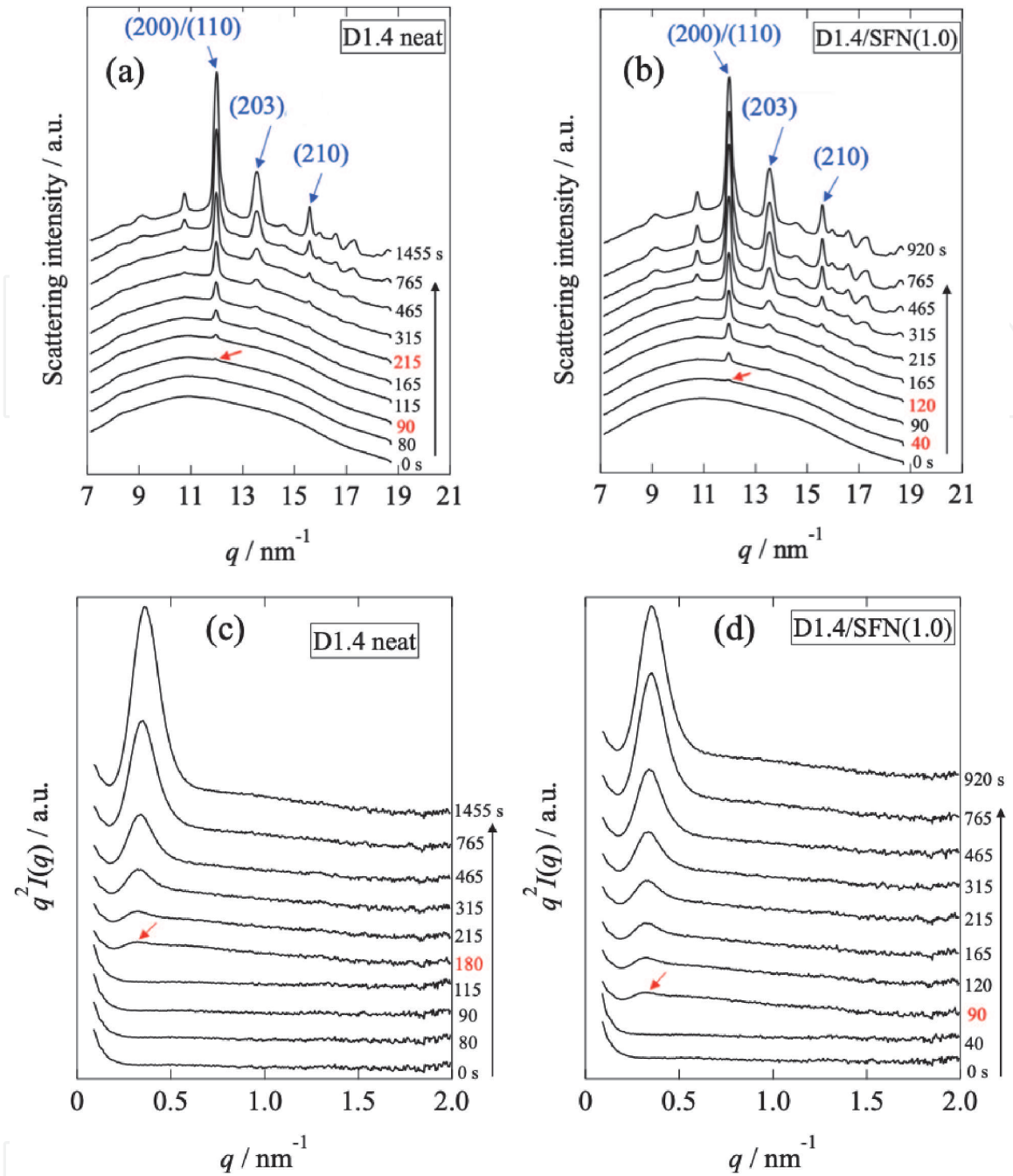


**Figure 5.** Time-resolved (a)-(b) WAXS and (c)-(d) Lorentz-corrected SAXS profiles of D1.4 neat and D1.4/SFN(1.0) specimens. The red arrow indicates the first detection of the peak (adapted from reference [9] with a permission).

proceeds, a crystalline peak appears at  $q = 11.96 \text{ nm}^{-1}$  (which has been shown by the red arrow). The induction period ( $t_0$ ) of the crystallization is evaluated from the first detection of the crystalline peak. It was found that loading of 1% SFN decreased the  $t_0$  from 90 s to 40 s, which shows that SFN enhanced the nucleation of PLLA.

The time evolution of the degree of crystallinity was calculated from the WAXS profiles by using the following equation

$$\phi_{\text{WAXS}} = \frac{\Sigma A_c}{\Sigma A_c + A_a} \quad (2)$$

Here,  $\Sigma A_c$  is the summation of the peak area of the crystalline peaks, and  $A_a$  is the peak area of the amorphous halo. The peak decomposition was conducted, and



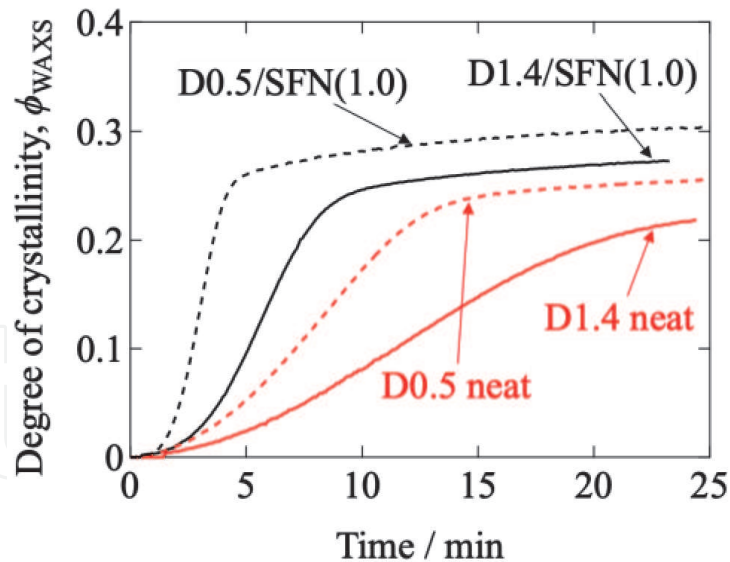


**Figure 6.**

Degree of crystallinity as a function of time for the isothermal crystallization at 110°C (adapted from reference [9] with a permission).

the degree of crystallinity  $\phi_{\text{WAXS}}$  was calculated, which is plotted as a function of crystallization time in **Figure 6**.

As can be seen in **Figure 6**, the final degree of the crystallinity has been increased and  $t_{0.5}$  is decreased by the inclusion of 1% SFN, indicating the acceleration of the crystallization rate.

**Figure 5(c)** and **(d)** show the changes in the Lorentz-corrected SAXS profiles as a function of time during the isothermal crystallization at 110°C for the D1.4 neat and D1.4/SFN(1.0) specimens. Here, the scattering intensity,  $I(q)$ , is corrected as  $q^2 I(q)$  by multiplying  $q^2$ . There was no SAXS peak observed in the early stage of crystallization. As time goes on, a clear scattering peak was observed at  $t = 180$  s for the D1.4 neat or  $t = 90$  s for the D1.4/SFN(1.0) specimen, which indicates the development of the lamellar stacking with sandwiching the amorphous layers. It is significant to observe that the SAXS peak appears later than the WAXS peak (**Figure 5**) which indicates that single lamellae (without stacking) are generated in the initial state of the PLLA crystallization from the melt.

As seen in **Figure 5(c)** and **(d)**, the SAXS peak moves towards the higher  $q$  as the crystallization proceeds. The long period ( $D$ ) of the lamellar stacks was evaluated from the peak position ( $q^*$ ) as  $D = 2\pi/q^*$ . As shown in **Figure 7(a)**, the  $D$  decreases as a function of the crystallization time which seemed to be conflicting to

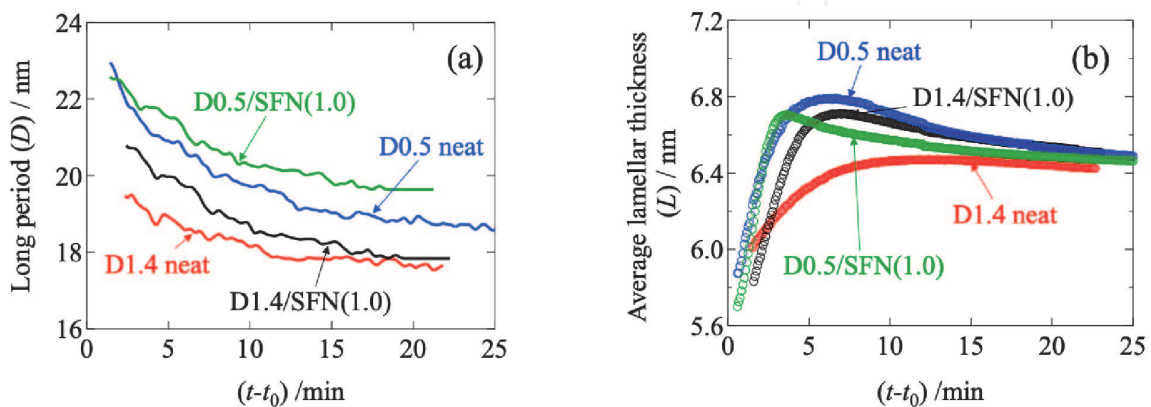


**Figure 7.**

SAXS results for isothermal crystallization at 110°C (a) long period ( $D$ ), (b) average lamellar thickness ( $L$ ) as a function of  $(t-t_0)$ , where  $t_0$  is the induction period (adapted from reference [9] with a permission).

the process of crystallization. To understand this behavior, the average thickness of the crystalline lamella ( $L$ ) was calculated from the SAXS profile through the correlation function [35]. The correlation function is expressed as:

$$\gamma(r) = \frac{\int_0^{\infty} I(q)q^2 \cos(qr) dq}{\int_0^{\infty} I(q)q^2 dq} \quad (3)$$

Here,  $\gamma(r)$  is the correlation function and  $r$  is the distance in the real space.  $\gamma(r)$  function was obtained from the comprehensive  $I(q)$  from  $q = 0$  to  $q = \infty$  by conducting the extrapolation of SAXS data for  $q \rightarrow \infty$  according to Porod's law and for  $q \rightarrow 0$ , Guinier's law is used. The detailed procedure is reported in Ref. [7]. **Figure 7(b)** shows thus-evaluated  $L$  as a function of time. As a result, the average lamellar thickness,  $L$  increases with time, which is reasonable as a crystallization behavior. Therefore, the decreasing behavior of  $D$  (as shown in in **Figure 7(a)**) is also reasonable, as schematically shown in **Figure 8**. Upon crystallization, shrinkage takes place. Since the lamella thickens with time, this results in the decrease of  $D$  (**Figure 8(b)** and **(c)**), as the amorphous layer thickness is decreased to a greater extent as compared to the increasing extent of  $L$  (lamellar thickness).

### 2.1.2 Cellulose nanocrystal (CNC)

In this section, we discuss the enhancement in PLLA crystallizability by the inclusion of marine green algae biomass residue (ABR) based additives, i.e., washed ABR (WABR) and the ABR extracted cellulose nanocrystal (CNC). The CNC was extracted from the waste of ABR by using acid hydrolysis method. The complete extraction and characterization process is reported in Ref. [14]. Apart from effect of CNC on the crystallization behavior of PLLA, we also compare the utility of waste ABR after washing, i.e., WABR (washed algae biomass residue) as a filler for PLLA. As reported

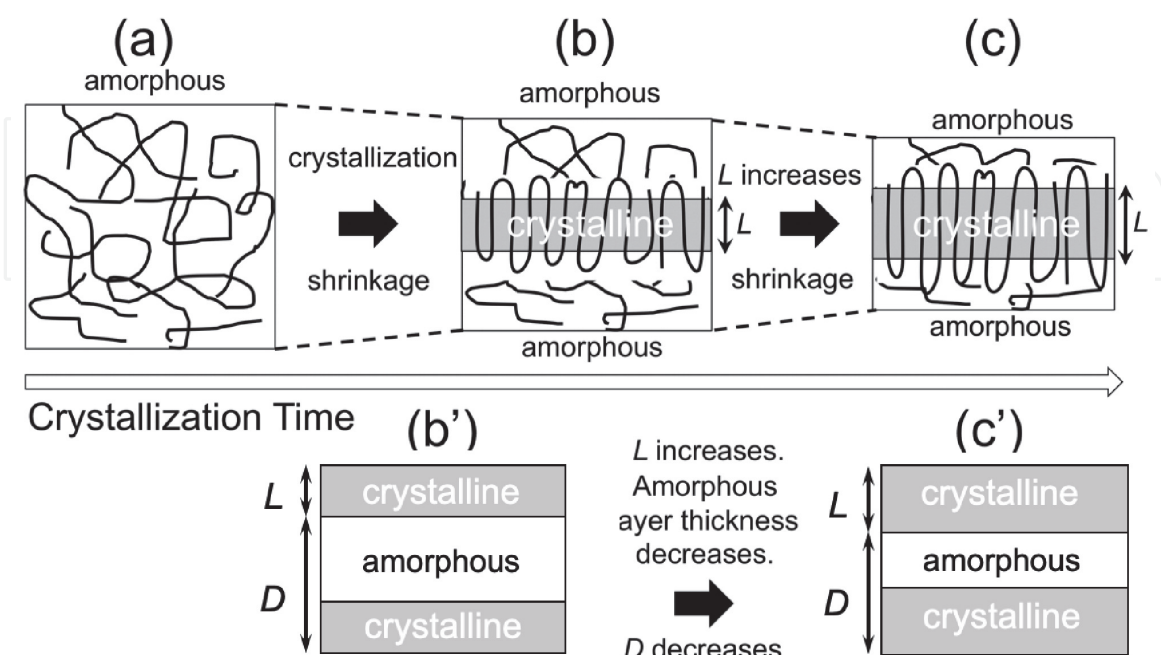


**Figure 8.** Schematic illustrations showing the change in the nanostructure upon crystallization of PLLA. (a) At the amorphous state before crystallization of the polymer melt, (b) in an early stage of crystallization, (c) lamellar thickening in the subsequent stage of the crystallization (adapted from reference [9] with a permission).

in Ref. [14] it was found that WABR had irregular morphology (micron size), while the CNC had needle-like morphology with an average diameter of 30–35 nm, and average length of 520–700 nm. [14]. PLLA/WABR and PLLA/CNC composites were prepared by solution casting method using chloroform as a solvent. The loading amount of the additives were 0.5%, 1%, and 2% by weight. The effects of WABR and CNC on isothermal crystallization of PLLA are discussed by DSC and POM.

**Figure 9** shows the degree of crystallinity as a function of time based on DSC results for the isothermal crystallization of neat PLA, PLA/WABR and PLA/CNC nanocomposites at 110°C. The degree of crystallinity ( $\phi$ ) was calculated by using Eq. (1). As shown in **Figure 9**, the addition of WABR, and CNC can improve the crystallizability of PLLA by reducing induction period, crystallization half-time, and by increasing the ultimate degree of crystallinity. It was observed that the CNCs were more effective as a crystallizing agent in comparison to WABR. Based on the DSC measurement in heating scan, it was found that WABR and CNC does not change the  $T_g$  and  $T_m$  of PLLA [14]. These results are similar to the case of loading SFN which is also a solid state additive [8].

**Figure 10** shows the representative POM images for the isothermal crystallization at 125 °C for the neat PLA, PLA/WABR(1.0), and PLA/CNC(1.0) specimens at  $t = 12$  min. First, negative spherulites were observed for all the specimens which shows that WABR and CNC had no effect on the structure of the PLA spherulites.

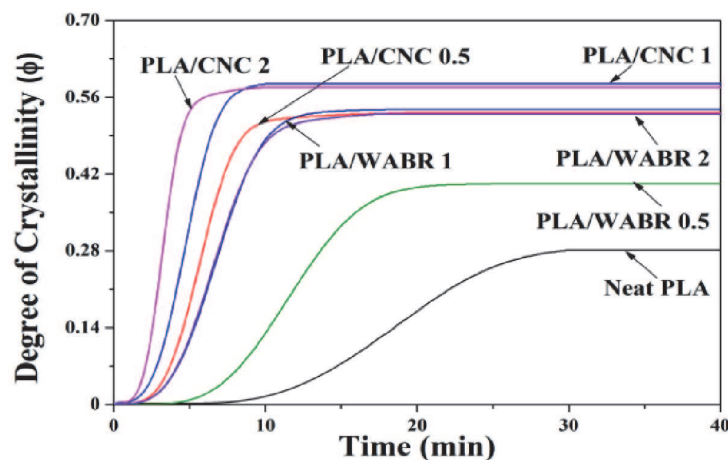


**Figure 9.** Degree of crystallinity as a function of time based on DSC results for the isothermal crystallization of neat PLA, PLA/WABR and PLA/CNC nanocomposites at 110°C. the degree of crystallinity ( $\phi$ ) was calculated by using Eq.(1) (adapted from reference [14] with a permission).

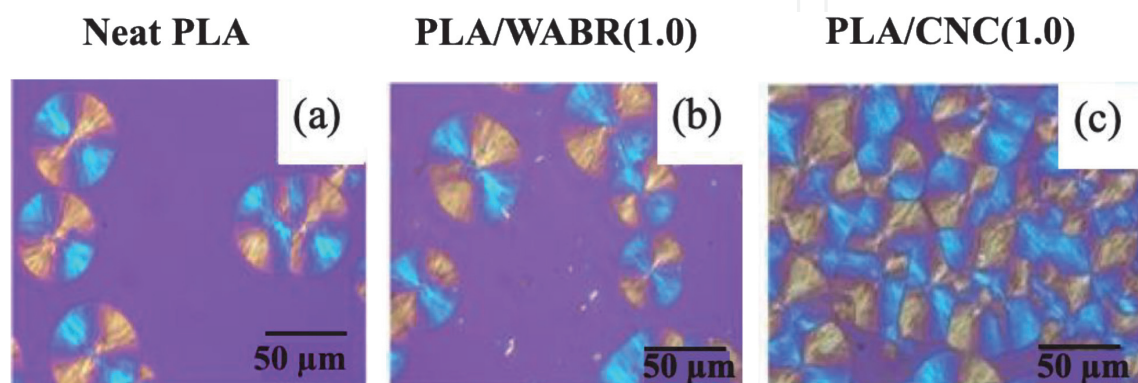


**Figure 10.** The representative POM images for the (a) neat PLA, (b) PLA/WABR(1.0), and (c) PLA/CNC(1.0) specimens for the isothermal crystallization at 125°C for  $t = 12$  min (adapted from reference [14] with a permission). The figure has been slightly modified.

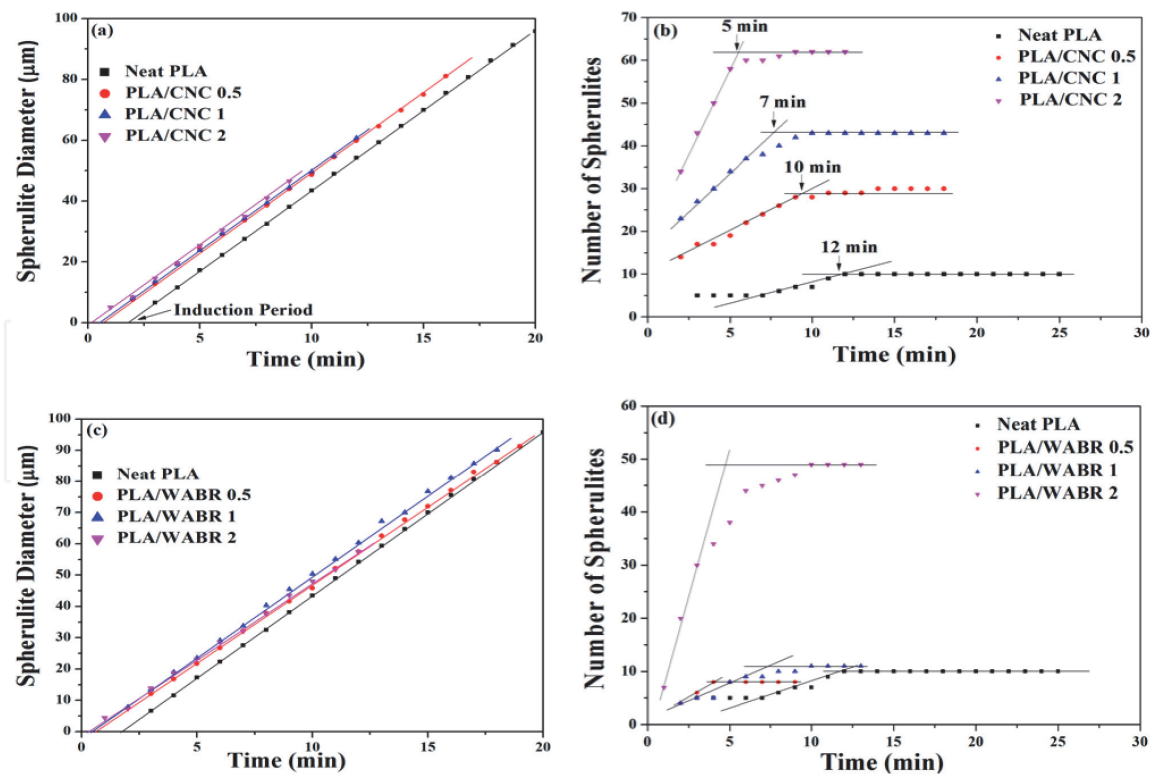


**Figure 11.** (a) Spherulite diameter, (b) number of spherulites in the PLA/CNC bio-nanocomposites, and (c) spherulite diameter, (d) number of spherulites in the PLA/WABR bio-composites as a function of time at an isothermally crystallized temperature of 125°C (adapted from reference [14] with a permission).

Furthermore, **Figure 11** shows the spherulite diameter, and number of spherulites as a function of time, which were calculated from the POM images. It was observed that the incorporation of WABR, and CNC into the PLA matrix accelerated the rate of nucleation, however, the growth rate of the PLA spherulite was almost unchanged. CNC was found to be more effective than the WABR. The needle-like morphology and high aspect ratio of CNC were mainly accountable for the better effectiveness on improvement in the crystallization of PLA. On the contrary, the larger particle size of WABR might be the possible reason for its less effectiveness.

The results shown in this section suggest that even the low loading amount of solid state additives can enhance the crystallization of PLLA by providing more sites for nucleation without altering  $T_g$ ,  $T_m$ , and spherulite growth during the isothermal crystallization from the melt.

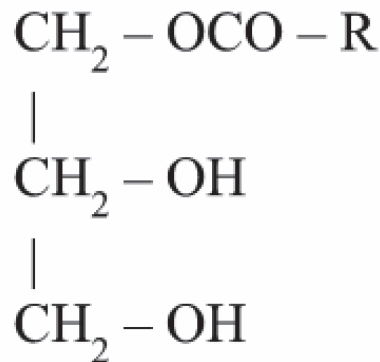
## 2.2 Liquid state additive (plasticizer)

In this section, we will focus on the enhancement in crystallizability of PLLA by using a special plasticizer (organic acid monoglyceride; OMG). The chemical structure of OMG is shown in **Figure 12**. OMG is a product of Taiyo Kagaku Co., Ltd. The commercial name of OMG is Chirabazol D, which is a biobased plasticizer. The OMG has a molecular weight of 500 and a melting temperature of  $T_m = 67^\circ\text{C}$ . PLLA/OMG specimens were prepared by the solution casting method, using chloroform as a solvent. The specimens are labeled as D1.4/OMG( $x$ ) or D0.5/OMG( $x$ ), where the numbers after D denote the % of D moiety in PLLA, and  $x$  stands for % of OMG inclusion.

**Figure 13** shows the effect of OMG on the glass transition temperature ( $T_g$ ) of PLLA. It is noticeably observed that  $T_g$  of PLLA decreases with the OMG content. More rigorously, we compare the result with the estimation by the plasticizing effect. The  $T_g$  can be simply estimated as.

$$T_g(\text{PLLA/plasticizer})(\text{K}) = \left(1 - \frac{\text{wt\% of plasticizer}}{100}\right) \times T_g(\text{neat})(\text{K}) \quad (4)$$

**Figure 13** shows the experimental  $T_g$  and the estimated  $T_g$  (with two straight lines) as a function of OMG content. The data points are almost in accord with the lines up to 1.0%, and then deviated from the lines above the OMG content of 1.0%. These results suggest that the OMG acts as a plasticizer for PLLA when the OMG loading is <1.0%. **Figure 14(a)** shows the DSC results of the isothermal crystallization of neat and 1% OMG loaded specimens at 110°C. The reduction in  $t_{0.5}$  in **Figure 14(b)** confirmed the enhancement in crystallization rate. **Figure 14(c)**



R: substituent group with  
380 molecular weight

**Figure 12.**  
Chemical structure of OMG.

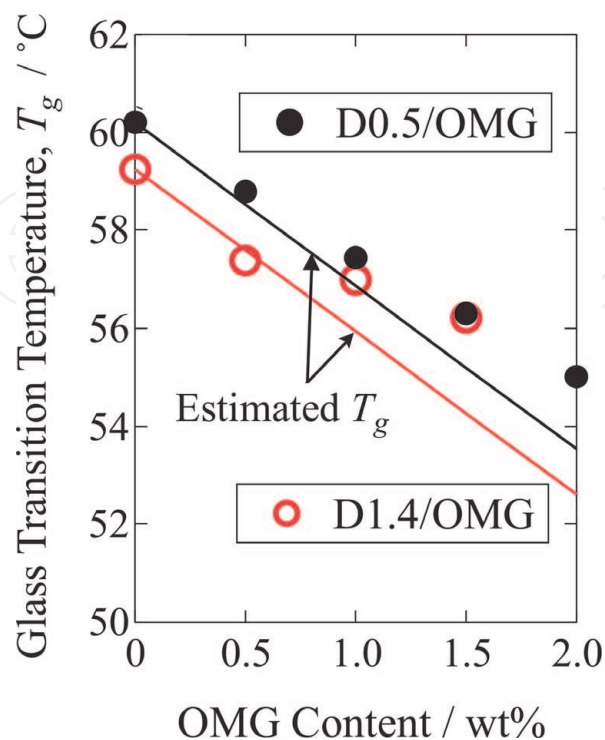


**Figure 13.**  
Glass transition temperature ( $T_g$ ) as evaluated from DSC curves. The lines show estimated  $T_g$  (adapted from reference [10] with a permission).

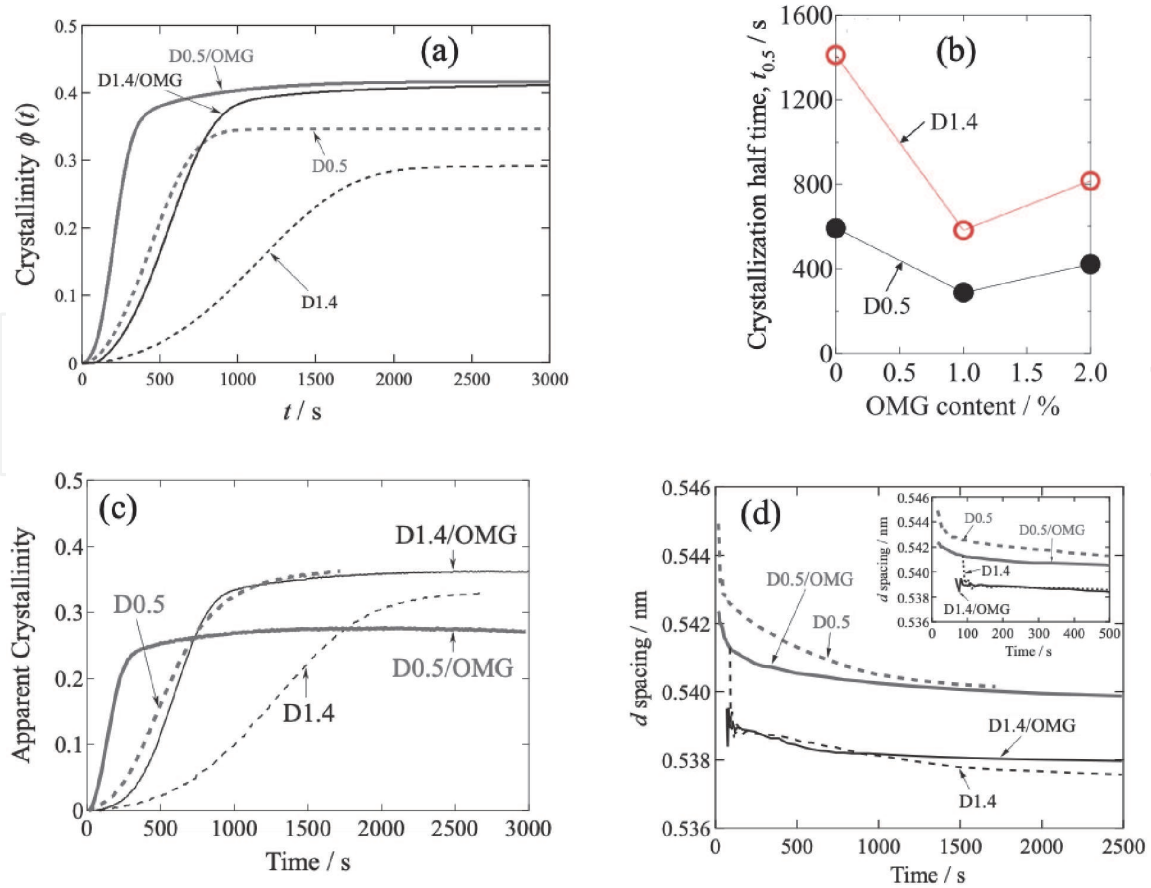


**Figure 14.** (a) DSC results for isothermal crystallization at 110°C (b) crystallization half-time as a function of OMG loading (c) apparent crystallinity based on WAXS results, and (d)  $d$  spacing as a function of time (adapted from reference [7] with a permission).

shows the apparent degree of crystallinity which was evaluated using Eq. (2), based on the WAXS results as a function of the crystallization time for all specimens. The effect of the OMG is very clear for the acceleration of crystallization.

**Figure 15(a)** shows the change in long period,  $D$  as a function of time during the isothermal crystallization at 110°C for neat and 1% OMG loaded specimens. The long period decreases as the crystallization proceeds which can be explained by **Figure 8**. Furthermore, **Figure 15(b)** shows changes in the lamellar thickness (calculated from SAXS profile through the correlation function,  $\gamma(r)$ ) as a function of

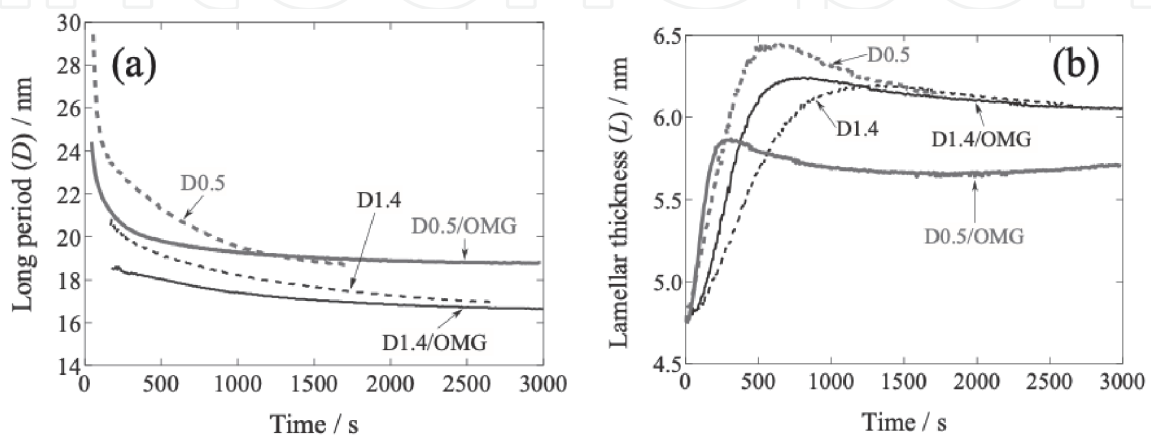


**Figure 15.** SAXS results for isothermal crystallization at 110°C (a) long period ( $D$ ), (b) lamellar thickness ( $L$ ) as a function of time (adapted from reference [7] with a permission).

time. As time proceeded, the lamellar thickness increased in the early stage and then leveled off in the later stage. These results suggest that the lamellar thickness increased quickly in the early stage of crystallization due to a decrease in the D-content and the addition of OMG. The ultimate lamellar thicknesses (at 3000 s) for all specimens are relatively similar, although the value for the D0.5/OMG is 0.94 times those of the others.

The time-resolved Lorentz-corrected SAXS profiles during isothermal crystallization at 100°C from the melt (200°C) for D1.4/OMG and D0.5/OMG specimens are shown in **Figure 16**. There was no SAXS peak observed in the early stage. As the crystallization proceeds, the SAXS peak appears which gradually shifts towards the higher  $q$  range. As can be seen in **Figure 16(b)**, there was observed a clear second peak in the higher  $q$  range for the D0.5/OMG(1.0) specimen. However, the position of the new peak is not twice of the position of the first-order peak which means that the new peak is independent of the first-order peak. This result correspond to the newly formed lamellar stacking. There are three possible models to account for the appearance of a new peak in the higher  $q$  range. One is the formation of new lamellar stacks in the amorphous region with much shorter long period, as schematically shown in **Figure 17(a)**. The second one is the new lamellar stacks formed perpendicular to the original lamellar stacks, as schematically shown in the **Figure 17(b)**. This model is referred to as the cross-hatched lamellae [36–38]. The third one is the insertion of a new lamella into the amorphous phase, which is sandwiched by the neighboring two preceding lamellae, as schematically shown in the **Figure 17(c)**. This kind of insertion of a new lamella has been considered by

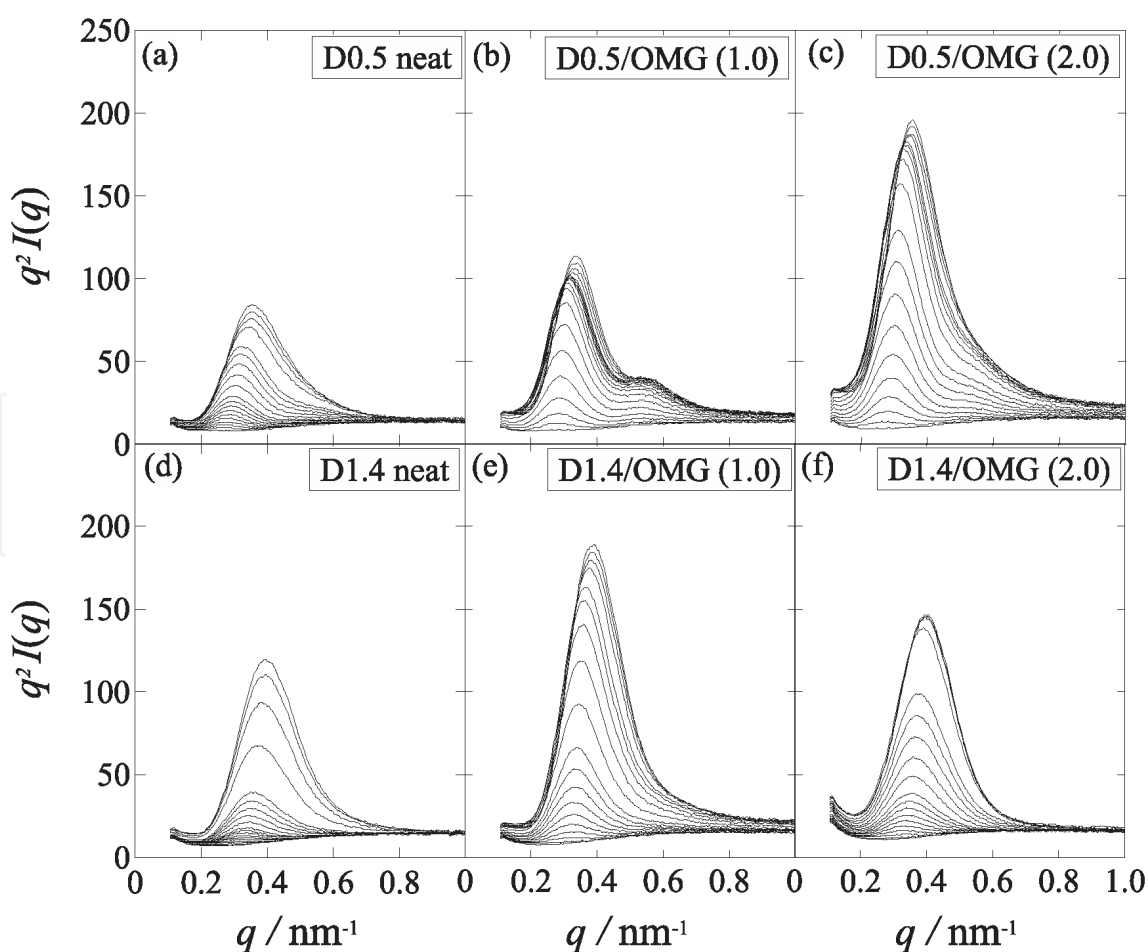


**Figure 16.** Temporal changes in the Lorentz-corrected SAXS profiles upon T-jump from 200 °C to 100 °C for the specimen (a) D0.5 neat, (b) D0.5/OMG(1.0), (c) D0.5/OMG(2.0), (d) D1.4 neat, (e) D1.4/OMG(1.0), and (f) D1.4/OMG(2.0) specimens (adapted from reference [10] with a permission).

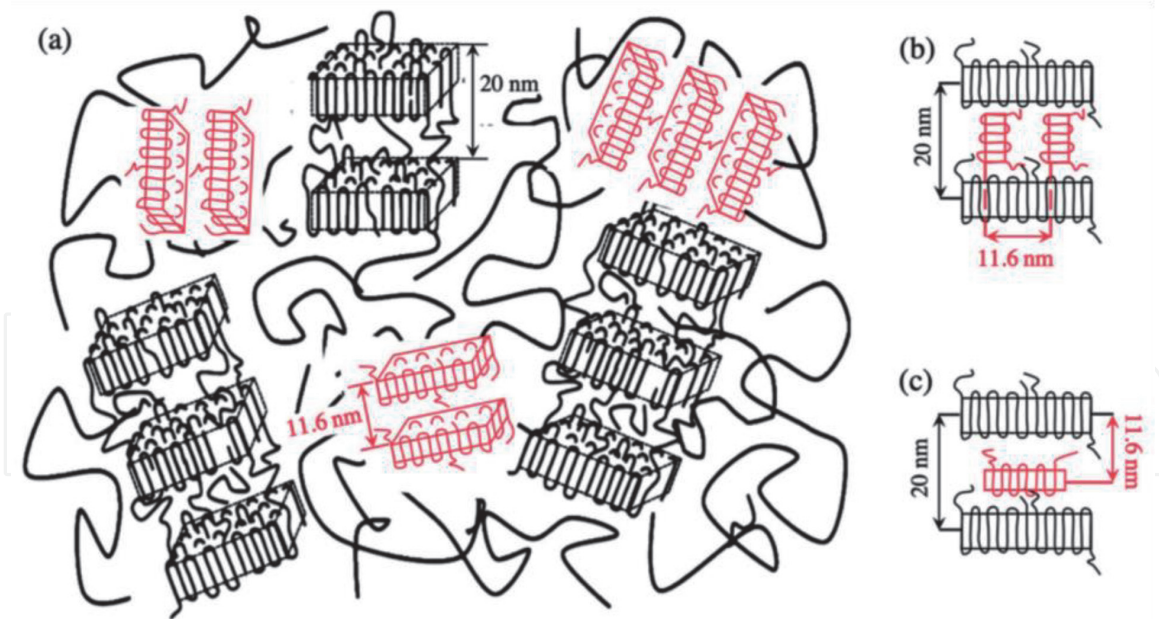


**Figure 17.** Schematic representation for the formation of a new lamellar stack. (a) Independent stacking, (b) formation of a new stack in the amorphous phase in between the original lamellae with the stacking direction perpendicular to each other (cross-hatched lamellae) and (c) insertion of a new lamella in between the original lamellae (adapted from reference [10] with a permission).

Hama et al. [39]. At present, it is difficult to specify which model is appropriate. Although there was no such peak observed for the D0.5/OMG(2.0) specimen, the shoulders are clearly observed for this specimen (**Figure 16(c)**). Therefore, even for this specimen the effect of OMG to induce such a new lamellar stack can be recognized.

The POM observations were conducted to count the number of the spherulites as a function of time during the isothermal crystallization at 130 °C. **Figure 18(a)** and **(b)** show the representative POM images for the isothermal crystallization at 130 °C for the D1.4 neat and D1.4/OMG(1.0) specimens at  $t = 29$  min. Since, the negative spherulites were observed which indicates that there is no effect of OMG on the structure of the spherulites. **Figure 18(b)** shows enhanced number of spherulites by loading of OMG which indicates that OMG can enhance the nucleation process of PLLA. From **Figure 18(c)**, it can be seen that the OMG enhances the spherulite growth of PLLA which clearly shows the effect of OMG to improve the crystallizability of PLLA. We speculate that the lowering of the activation energy for the PLLA crystallization may be the main effect of the OMG [10].

### 3. Enhancement in stereocomplex crystallization of PLLA/PDLA blend

In this section, the PLLA/PDLA (50/50) blends were prepared by solution casting method. Firstly, the PLLA and PDLA solutions were separately prepared with a concentration of 5% (w/v), using dichloromethane (DCM) as a solvent. The SFN was dispersed in DCM by using the ultrasonication method as discussed in the reference [8]. The PLLA, PDLA solutions, and the SFN dispersion, all together were mixed in one glass vessel and stirred for 12 h. The loading of SFN was 1% with the weight ratio of PLLA, PDLA, and SFN as 49.5/49.5/1.0. After the mixing, the solution was poured into a Petri dish for solvent evaporation at RT. After complete evaporation of the solvent, the as-cast films were obtained which were further dried in a vacuum oven at 50°C for 24 h. The specimens are labeled as LD neat and



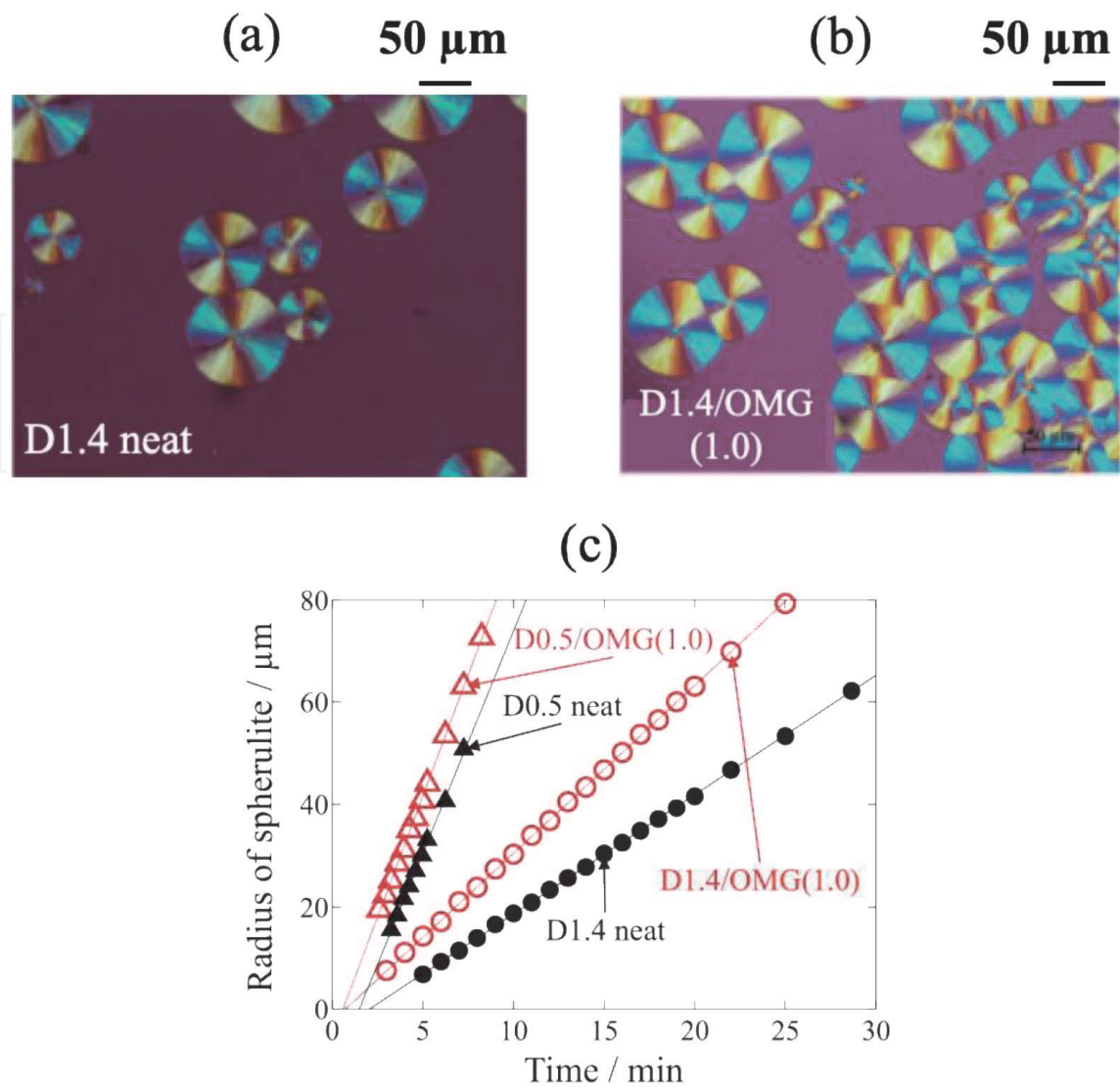


**Figure 18.**

(a), (b) POM images for the D1.4 neat and D1.4/OMG(1.0) specimens for the isothermal crystallization at 130°C for  $t = 29$  min. (c) Plots of the radius of spherulite vs. time evaluated from the results of POM (adapted from reference [10] with a permission). The figure has been slightly modified.

LD/SFN(x), where LD denotes the blend of PLLA/PDLA(50/50), and x denotes the % loading of SFN.

Prior to the study of the effect of SFN on the crystallization of PLLA/PDLA (50/50) blend, we checked the effect of SFN on PDLA crystallization as SFN was known to improve the crystallization of PLLA (see Section 2.1.1). **Figure 19** shows the comparison of degree of crystallinity during isothermal crystallization of PLLA neat, PLLA/SFN(1.0), PDLA neat, and PDLA/SFN(1.0) specimens at 110°C. It can be seen from this figure that the ultimate degree of crystallinity ( $\phi^\infty$ ) at the isothermal crystallization temperature of 110°C is increased by adding 1% SFN in PLLA or PDLA specimen. As shown in **Figure 19** the induction period,  $t_0$  and the crystallization half-time,  $t_{0.5}$  of the PDLA neat specimen are shorter than those of the PLLA neat specimen. This may be because the optical purity of the PDLA sample (D-content >99.5%) is higher than that of PLLA sample (L-content = 99.5%), as we know that the nucleation and crystallization of PLA (PLLA or PDLA) becomes quicker with the increasing optical purity. By adding SFN, the  $t_0$  was almost unchanged for the case of the PDLA/SFN(1.0) specimen, while it was significantly decreased for the case of PLLA/SFN(1.0), furthermore, the  $t_{0.5}$  is decreased for both cases. It was much decreased for the case of PLLA than that of PDLA, ensuring the

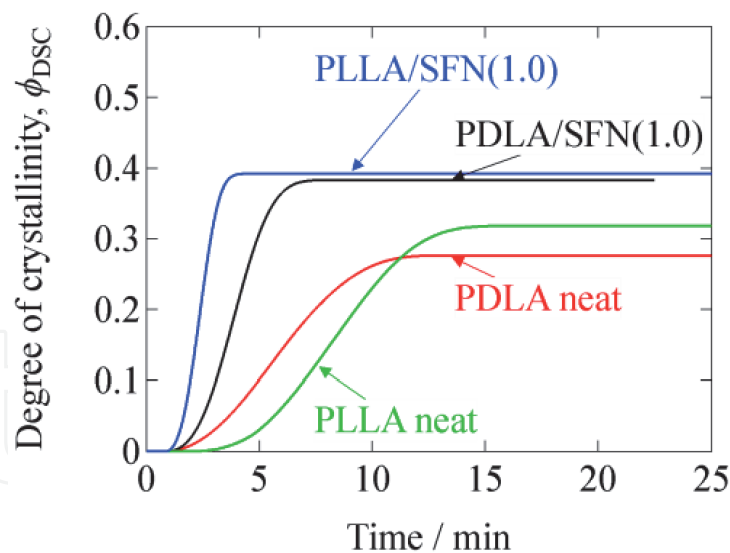


**Figure 19.**

Degree of crystallinity ( $\phi_{DSC}$ ) as a function of time, which was evaluated based on the heat flow results (adapted from reference [15] with a permission).

superior SFN effect due to its similarity of the chemical structure to PLLA. These results indicate the enhancement in the crystallizability of PDLA by adding 1% SFN, although SFN is much effective for the improvement of crystallizability of PLLA.

For the isothermal crystallization from melt, we set the melt temperature at 260°C for 5 min and then immediately quench to 110°C or 170°C and hold it isothermally until the crystallization completes. The reason why we selected 110°C is that it was found in **Figure 4** that the rate of crystallization of PLLA HC crystal is maximum at ~110°C. This is the best temperature to achieve the maximum amount of crystallinity of PLLA which is desirable for industrial purposes.

Furthermore, since at 110°C the formation of HC and SC occurs simultaneously so to see the effect of SFN on the formation of SC crystals solely, we conducted the isothermal crystallization at 170°C because at this temperature HC crystals cannot form ( $T_{m,HC} = 170 \sim 180^\circ\text{C}$ ) due to the shallow quench depth ( $\Delta T = T_m^O - T_c$ ).

The effect of SFN on the isothermal crystallization behavior of the PLLA/PDLA blend specimen was investigated at  $T_{iso} = 110^\circ\text{C}$ . **Figure 20** shows the DSC results of the isothermal crystallization of LD neat and LD/SFN(1.0) specimens at 110°C from the melt (260°C). In **Figure 20(a)**, the heat flow as a function of time at the isothermal crystallization temperature is plotted. Adding 1% SFN, the crystallization exothermic peak shifts to the shorter time, showing an enhancement in the crystallization speed. However, it was not possible to distinguish the evolution of HC and SC phases from the plots of **Figure 20(a)**. To see the crystallites formed in the isothermal crystallization, the subsequent heating is conducted after the complete crystallization at 110°C. **Figure 20(b)** shows the results of the DSC heating scan. It is seen that by adding 1% SFN the  $\Delta H_{m,HC}$  and  $T_{m,HC}$  decreased and the  $\Delta H_{m,SC}$  and  $T_{m,SC}$  increased. These results indicate that the SFN can enhance the formation of SC and can suppress the formation of HC. The change in the melting temperature indicates that the presence of SFN may increase the lamellar thickness of the SC crystals while the lamellar thickness of HC crystals may be decreased due to the suppression of the HC crystallization. The increase in the melting point of SC is helpful to increase the thermal stability of PLA.

The effect of SFN on the isothermal crystallization behavior of the PLLA/PDLA blend specimen at 170°C was studied by the DSC measurement as shown in **Figure 20(c)**. Since the temperature 170°C is too high for the formation of HC ( $T_{m,HC} = 170 \sim 180^\circ\text{C}$ ), only the formation of SC can be considered at this

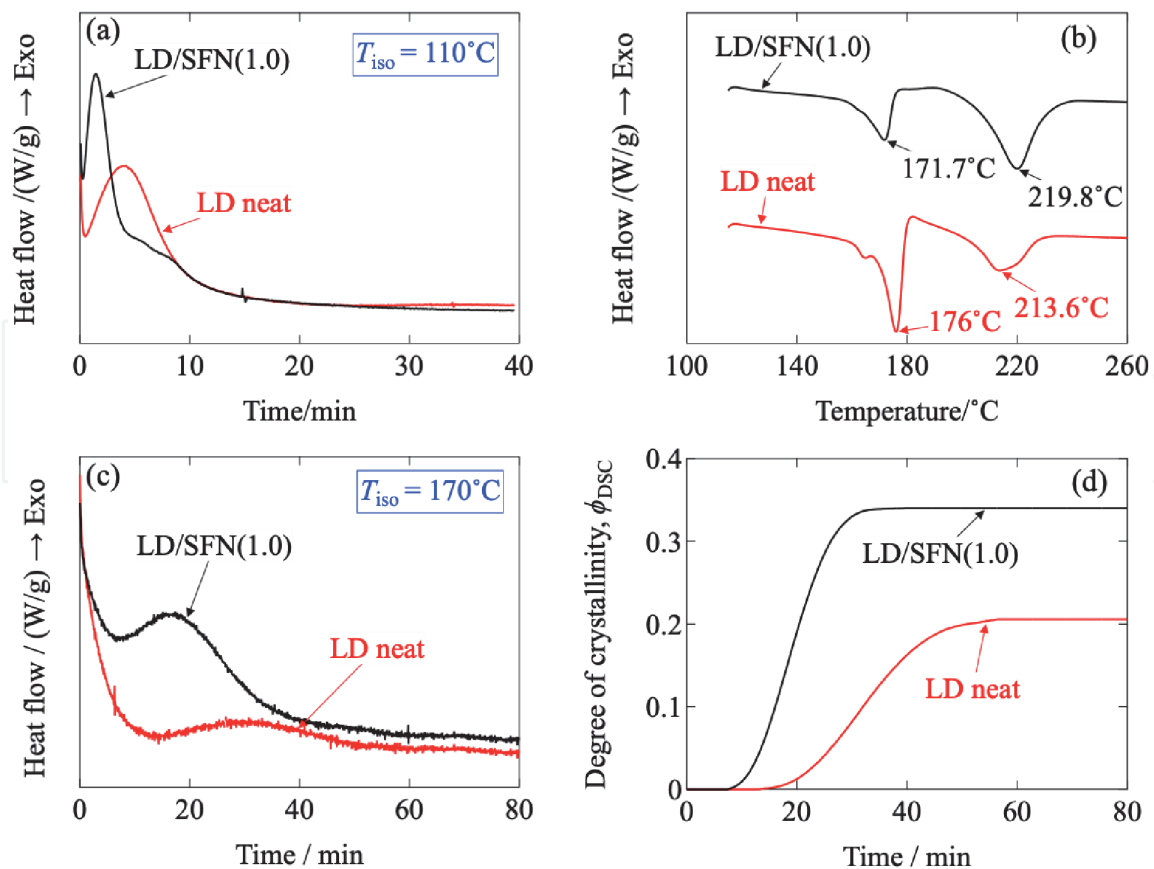


**Figure 20.**

(a) Heat flow as a function of time during the isothermal crystallization at 110°C from the melt (260°C), and (b) the subsequent heating scan from 110–260°C with the rate of 20°C/min. (c) Heat flow curves as a function of time during the isothermal crystallization at 170°C from the melt (260°C), and (d) changes in the degree of crystallinity ( $\phi_{DSC}$ ) as a function of time at 170°C, (adapted from reference [15] with a permission).

temperature (see later WAXS results in **Figure 21(c)** and **(d)**). From **Figure 20(c)** and **(d)**, it is clearly seen that the ultimate degree of crystallinity at the isothermal crystallization temperature of 170°C is increased by the presence of SFN. The  $t_0$  was decreased from 13 min to 7.4 min and the  $t_{0.5}$  was also decreased from 32.3 min to 19.1 min. These results indicate the enhancement in the stereocomplex crystallization of PLLA/PDLA (50/50) blend specimens by adding 1% SFN.

To clearly distinguish the evolution of HC and SC during the isothermal crystallization, we conducted the time-resolved WAXS measurements at 110°C upon T-jump from 260°C. **Figure 21(a)** and **(b)** show the change in WAXS profiles for the LD neat and LD/SFN(1.0) specimens as a function of time at 110°C. The peaks located at  $q = 8.75, 14.6,$  and  $16.6 \text{ nm}^{-1}$  belong to the SC crystals while the other reflection peaks belong to the HC. As shown in **Figure 21(a)**, even at the very early stage the  $SC_{(110)}$  reflection peak was observed for both the specimens, while the peak area of  $SC_{(110)}$  was much larger for the case of LD/SFN(1.0) specimen. The shorter induction period of SC than HC is due to the fact that the nucleation of SC is faster than that of HC in PLLA/PDLA (50/50) blend by the difference in the thermodynamic driving force of the crystallization. ( $\Delta T_{SC} > \Delta T_{HC}$  where  $\Delta T_{SC} = T_{m, SC} - T$  and  $\Delta T_{HC} = T_{m, HC} - T$ ). As time goes on, the HC peak appears at 125 s. It is noteworthy to observe here that the induction period of HC is unchanged by adding SFN. The time evolution of the degree of crystallinity was calculated from the WAXS profiles which is plotted as a function of time in **Figure 22**. As can be seen from **Figure 22** for the case of LD neat specimen, the HC peak appears later than the SC peak while it keeps on increasing and finally,  $\phi_{HC}$  overcomes  $\phi_{SC}$ . For the case of LD/SFN(1.0) specimen, the SC crystallization is much accelerated

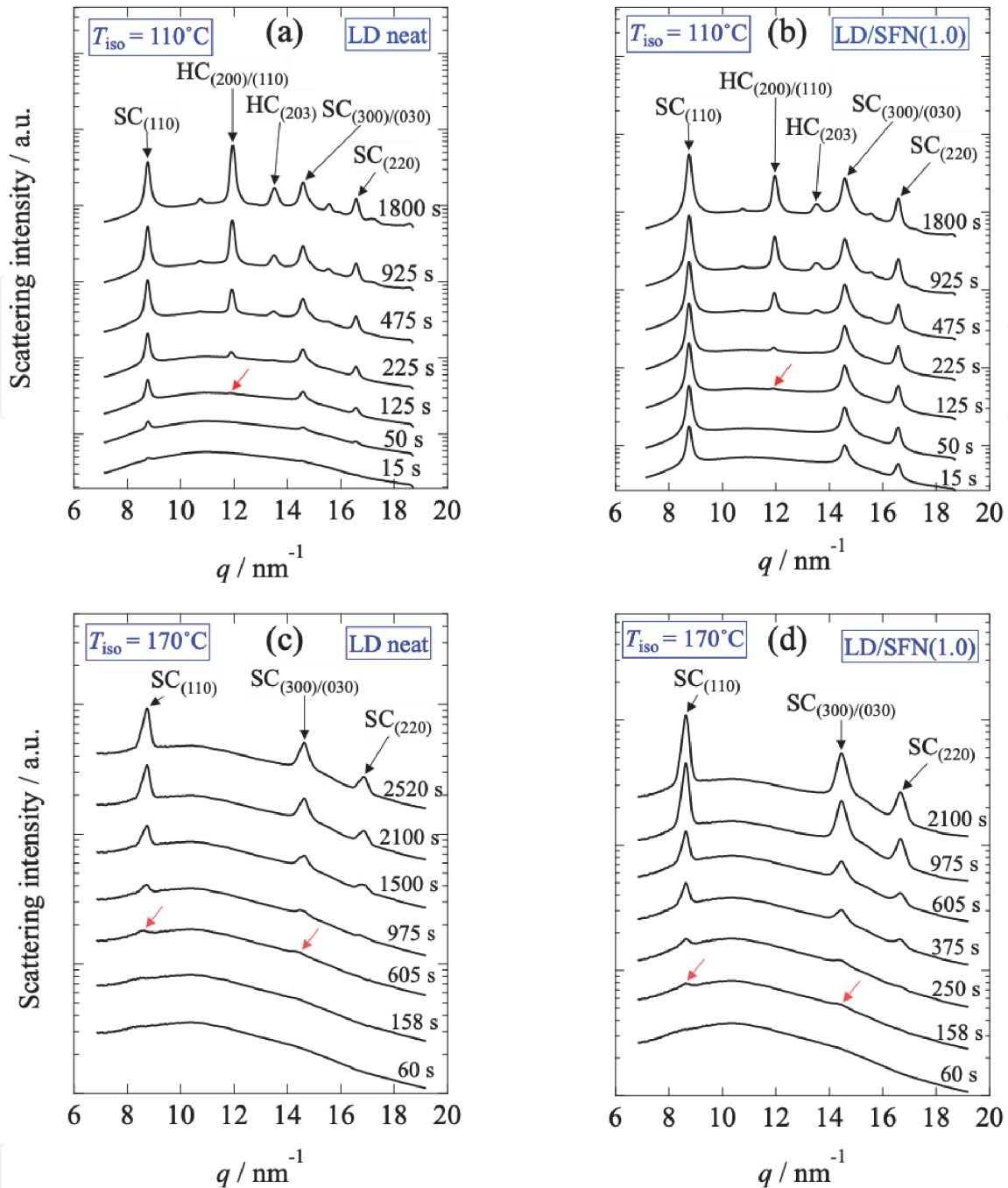


**Figure 21.** Time-resolved WAXS profiles after the T-jump from 260–110°C for (a) LD neat (b) LD/SFN(1.0) specimens. (the red arrow indicates the first detection of the peak for the HC). (c) Time-resolved WAXS profiles after the T-jump from 260–170°C for (c) LD neat (d) LD/SFN(1.0) specimens. (the red arrow indicates the first detection of the SC peak) (adapted from reference [15] with a permission).

in the very early stage with the almost zero induction period and in the final stage  $\phi_{HC} \ll \phi_{SC}$ . The fraction of SC ( $f_{SC}$ ) is increased after loading of 1% SFN while the total degree of crystallinity ( $\phi_{HC} + \phi_{SC}$ ) is unchanged at 30 min.

The average crystallite size ( $D_{hkl}$ ) in the direction normal to the ( $hkl$ ) plane was evaluated by Scherrer's Equation [40].

$$D_{hkl} = \frac{K\lambda}{\beta_{hkl} \cos\left(\frac{\theta}{2}\right)} \quad (5)$$

where  $K$  is a constant (0.9) and  $\lambda$  is the wavelength of the incident X-ray.  $\beta_{hkl}$  is a full-width at half maximum (FWHM) in the unit of radian, and  $\theta$  is the scattering

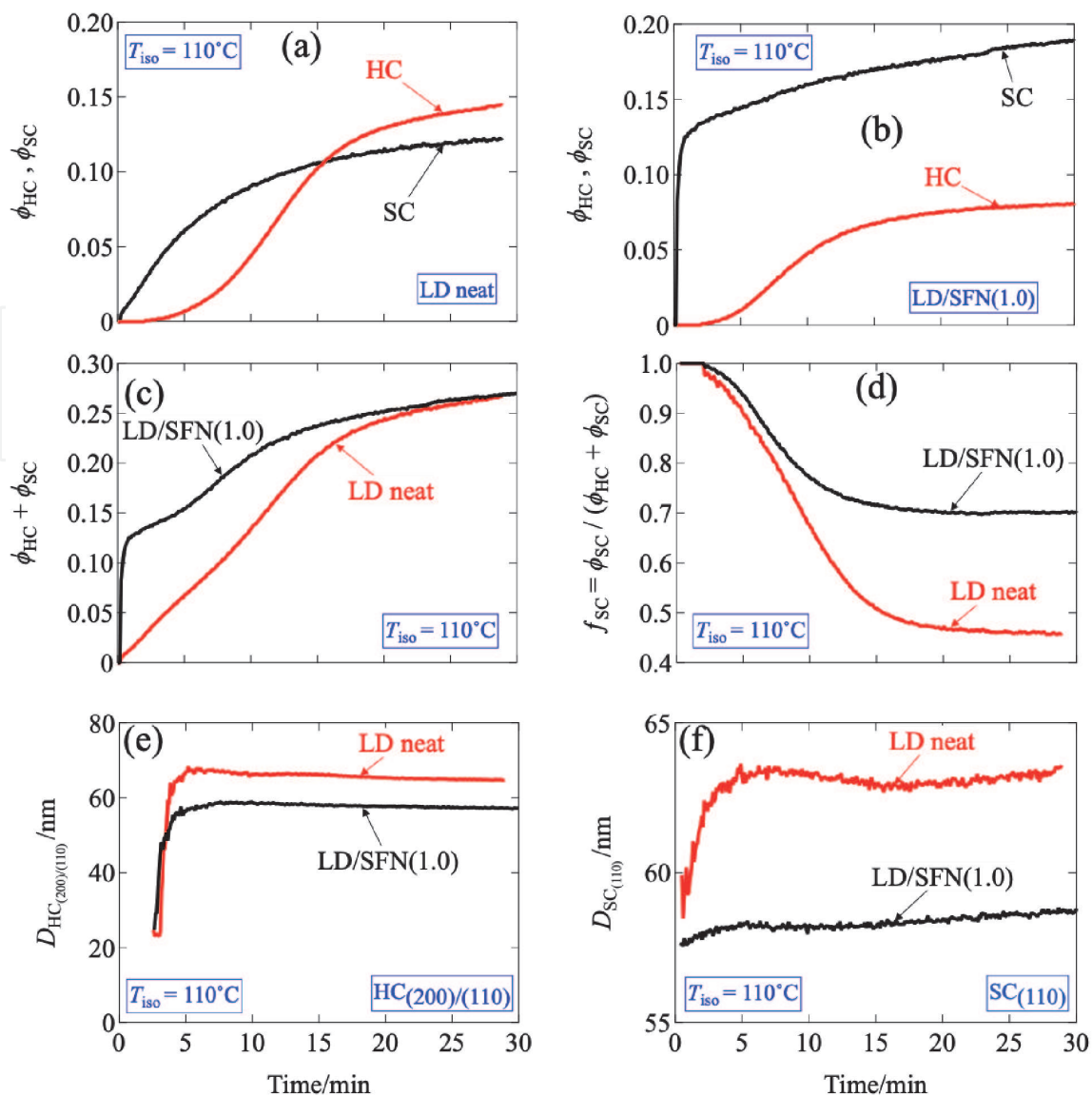


**Figure 22.**

Degree of crystallinity calculated from the results of **Figure 21** for (a) LD neat and (b) LD/SFN(1.0) specimens. (c) Total (HC + SC) degree of crystallinity and (d) fraction of SC as a function of time. Plots of average crystallite size as a function of time evaluated by Scherrer's equation for (e) HC and (f) SC (adapted from reference [15] with a permission).

angle. Note here that the raw data were used as the  $\beta_{hkl}$  values without correction for the peak broadening due to the collimation error of the WAXS setup, if any.

As seen in **Figure 22(e)** and **(f)**, the crystallite size is initially increasing as a function of time and it levels off after 5 min elapsed from the onset of crystallization. The slope of the plots in **Figure 22(e)** and **(f)** can be considered as the crystallite growth rate. Then, it can be stated that the growth rate of the HC crystallites is unchanged by the addition of SFN. The final value of the size of the HC crystallite for LD/SFN(1.0) specimens is slightly smaller than that in the LD neat specimen due to the effect of the SFN loading. As can be seen from **Figure 22(f)**, the size of the SC crystallite in the LD/SFN(1.0) specimen is much smaller than those of the LD neat specimen. Furthermore, it is interesting to notice that the initial size of the SC crystallite is the same for both the LD neat and the LD/SFN(1.0) specimens (**Figure 22(f)**).

To check the effect of SFN loading on the formation of SC crystals solely, we conducted the time-resolved WAXS measurements at 170°C. The changes in the WAXS profile were measured in the isothermal crystallization process at 170°C from the melt (260°C). **Figure 21(c)** and **(d)** show the WAXS profile for the LD

neat and LD/SFN(1.0) specimens as a function of time. It is also clearly shown that there is no peak for HC crystals which is due to such a high temperature, i.e. 170°C. It can be said that at 170°C only SC crystal formation takes place.

**Figure 23(a)** and **(b)** show the changes in Lorentz corrected SAXS profiles as a function of time during isothermal crystallization at 110°C for the LD neat and LD/SFN(1.0) specimens. The SAXS profiles in **Figure 23(a)** and **(b)** show the scattering from both the HC and SC crystal (as evidenced by WAXS results in **Figure 21**). To distinguish the contribution of HC and SC crystal, we conducted the peak decomposition of the SAXS profiles. The detailed procedure about the peak

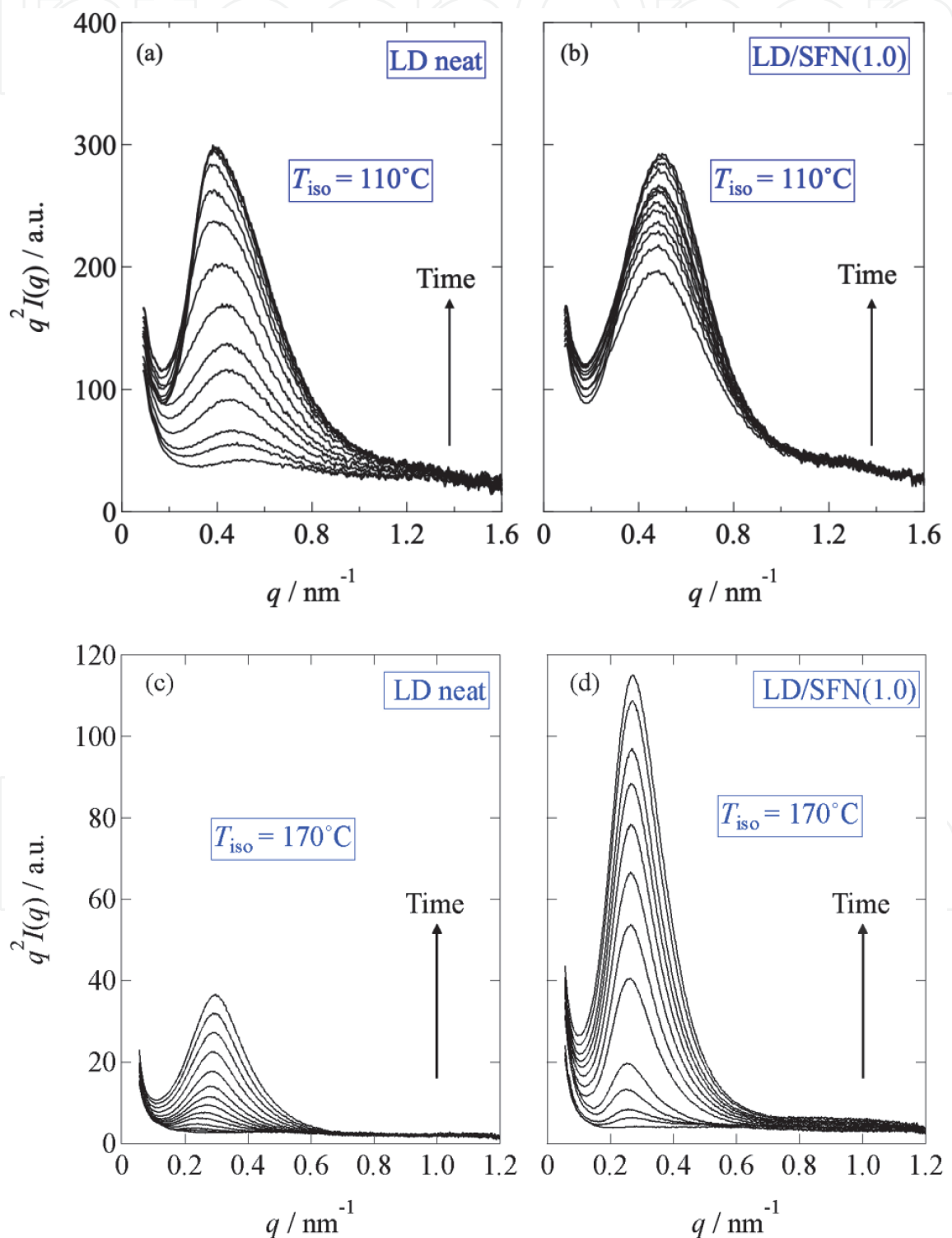


**Figure 23.** Changes in the Lorentz-corrected SAXS profiles as a function of time for LD neat and LD/SFN(1.0) specimens during the isothermal crystallization at (a)-(b) 110°C and (c)-(d) 170°C from the melt (260°C) (adapted from reference [15] with a permission).

decomposition is mentioned in Ref. [15]. For  $t < 6$  min, the SAXS profiles are symmetric which belong to SC crystals. As time goes on, after  $t = 6$  min, the second peak appears which shows the scattering from HC crystals. From the peak position ( $q^*$ ), the long period ( $D$ ) of the lamellar stacks was evaluated as  $D = 2\pi/q^*$ .

**Figure 24(a)** shows the plot of  $D$  as a function of time for the LD neat and LD/SFN (1.0) specimens which show the contribution of HC and SC separately. As seen in **Figure 24(a)**,  $D$  decreases as a function of time for HC crystals in the LD neat specimen. After loading 1% SFN, a similar trend was observed while the value of  $D$  of the HC lamellar stack was smaller than that of the LD neat specimen. The  $D$  of the SC lamellar stack in the LD neat specimen first increases up to  $t = 6$  min and then decreases after  $t > 6$  min. Considering **Figure 22(a)**,  $t = 6$  min can be taken as  $t_{0.5}$  (crystallization half-time). Then, the crystallization was quick in the stage  $t < t_{0.5}$ . Namely,  $D$  increased with time during the rapid crystallization while  $D$  decreased with time during the subsequent slow crystallization. **Figure 22(f)**, also suggests that the lateral size of SC lamellae was very rapidly increased for  $t < 6$  min. Therefore, it can be considered that the SC lamellae grow in their lateral direction by folding the polymer chains in the amorphous region outside of the lamellar stacks. In the meantime, thickening of the lamellae can be considered during this stage ( $t < t_{0.5}$ ). Namely, the lamellar thickening may be considered to take place by including the amorphous chains from outside of the lamellar stack. This situation quite differs from **Figure 8**, for which  $D$  is explained to be decreasing with time because of shrinkage in volume upon crystallization. As for the current case, no change in the amorphous layer with increasing of the thickness of the crystalline lamellae result in increasing the long period,  $D$ . For the LD/SFN(1.0) specimen  $D$  of the SC lamellar stack decreases from the beginning however the decreasing tendency became more evident for  $t > 6$  min.

**Figure 23(c)** and **(d)** show the changes in Lorentz corrected SAXS profiles as a function of time during isothermal crystallization at  $170^\circ\text{C}$  for the LD neat and LD/SFN(1.0) specimens. The intensity of the peak observed at  $q = 0.29 \text{ nm}^{-1}$  increases as a function of time. As seen in **Figure 23(c)** and **(d)**, the SAXS peak moves towards the higher  $q$  as the crystallization proceeds. Increase in  $q$  suggests the decrease in  $D$  as shown in **Figure 24(b)**. It can be seen that the long period,  $D$  decreases by the loading of SFN.

POM observations were conducted to evaluate the spherulite growth rate and the nucleation density as a function of time. The POM images of the evolution of spherulites for the LD neat and LD/SFN(1.0) specimens at  $170^\circ\text{C}$  as a function of

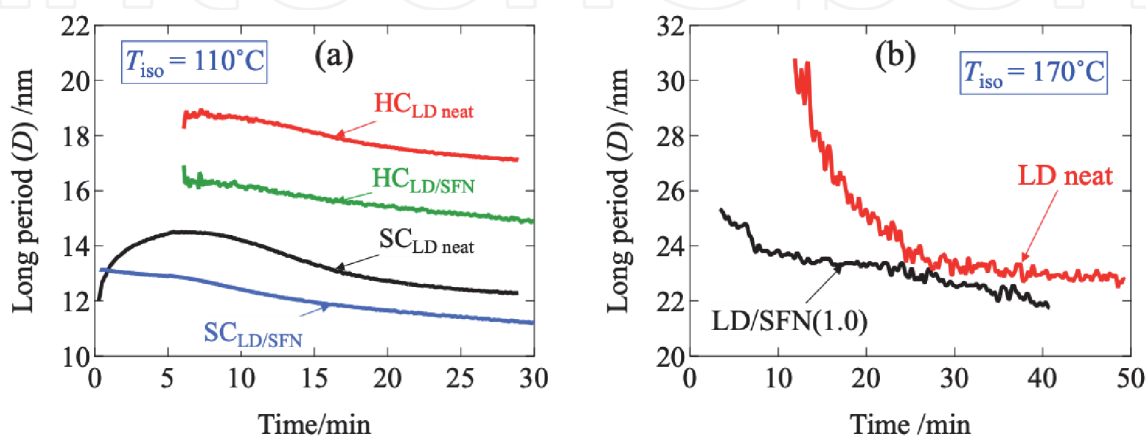


**Figure 24.**

Plots of long period ( $D$ ) as a function of time during the isothermal crystallization at (a)  $110^\circ\text{C}$  and (b)  $170^\circ\text{C}$  from the melt ( $260^\circ\text{C}$ ) (adapted from reference [15] with a permission).

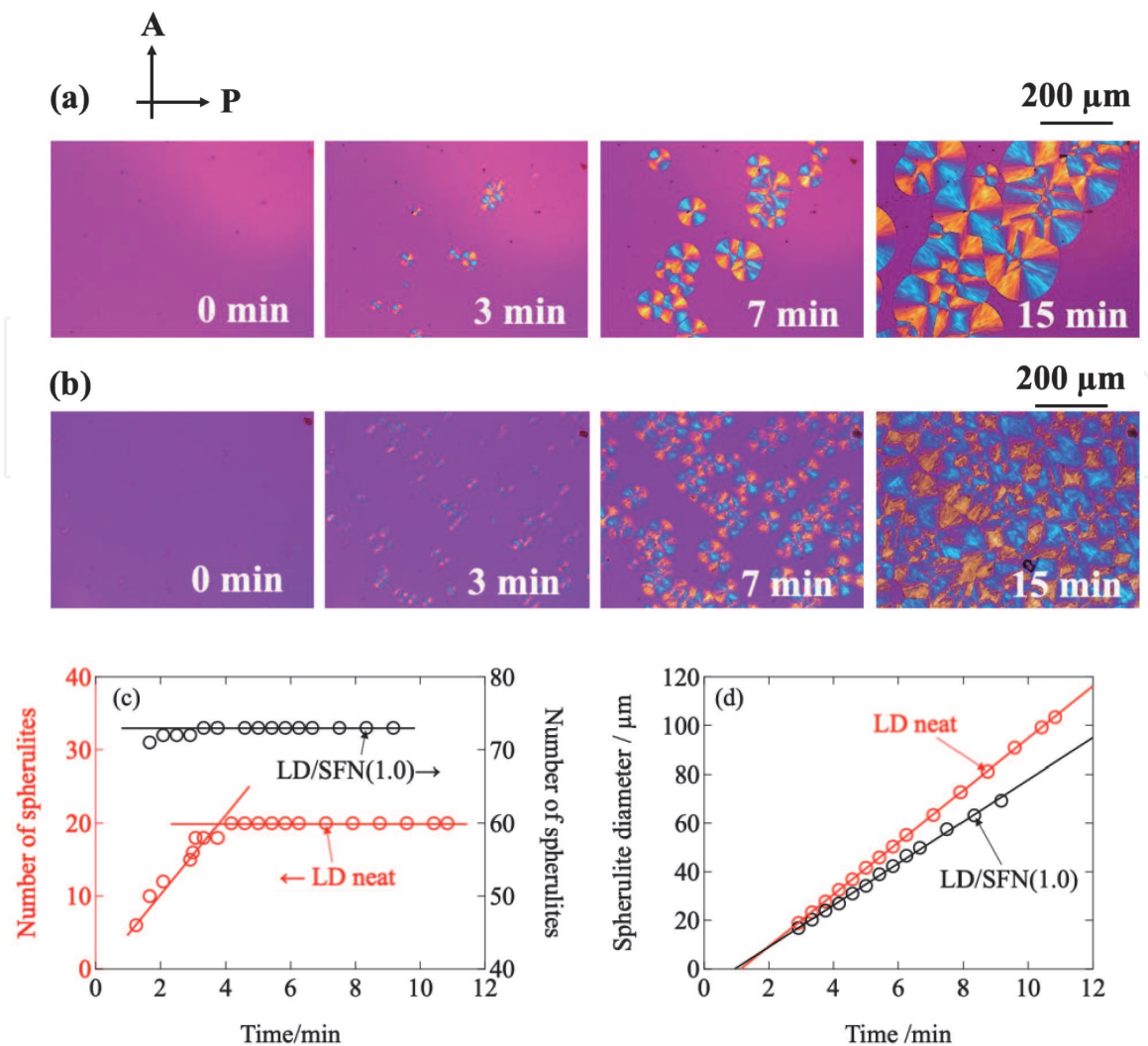


**Figure 25.** POM images as a function of time for the isothermal crystallization at 170°C for (a) LD neat (b) LD/SFN (1.0) specimens. (c) Changes in the number of spherulites as a function of time, (d) the plots of spherulite diameter as a function of time during isothermal crystallization at 170°C, evaluated from the POM images (adapted from reference [15] with a permission).

time are shown in **Figure 25(a)** and **(b)**. First, negative spherulites were observed with the typical Maltese-cross patterns for both of the LD neat and LD/SFN(1.0) specimens. The number of spherulites and the spherulite diameter as a function of time are plotted in **Figure 25(c)** and **(d)**. As shown in **Figure 25(c)** the number of spherulites increases as a function of time for the LD neat specimen below 4 min, suggesting homogeneous nucleation. In contrast, for the case of LD/SFN(1.0), the number of spherulites significantly increases and kept constant as a function of time (**Figure 25(d)**), suggesting heterogeneous nucleation due to the nucleation effect of SFN. The final number of spherulites increased approximately 3.6 times (from 21 to 73) upon the addition of SFN. Based on these results, SFN is considered as a nucleation agent for SC nuclei. The induction period calculated from **Figure 25(c)** looks unchanged. Furthermore, as seen in **Figure 25(d)** the growth rate (8.6 μm/min) of the spherulites in the LD/SFN(1.0) specimen is smaller than that of the spherulites in the LD neat specimen (10.7 μm/min). Although the growth rate of the SC crystals is decreased by the loading of SFN, the ultimate degree of crystallinity at 170°C (see **Figure 20(d)**) is increased by the loading of SFN. The slower growth of SC spherulites by adding SFN seems conflicting with the larger nucleation effects of SFN. These two conflicting results (as shown in **Figure 25(c)** and **(d)**) induced by the SFN loading are worthy of future research.



#### 4. Confined crystallization of PEG inside the preformed PLLA spherulite

In this section, we focus on the confined crystallization of PEG inside the preformed PLLA spherulite. The PLLA sample used in this study is the product of NatureWorks (code 4032D, D-content = 1.4%). The PEG sample was purchased from Wako Pure Chemical Industries, Ltd., of which  $M_w$  is 20,000. The PLLA/PEG (50/50) blend specimen was prepared by the solution casting method, using DCM as a solvent to obtain a solution with ca. 5 wt% of the total polymer concentration. The polymer solution was then poured into a Petri dish for complete evaporation of DCM.

The PLLA/PEG (50/50) blend specimen was heated up to 180.0°C and kept at this temperature for 5 min to obtain complete melt without liquid–liquid phase separation. Then, a two-step temperature-jump was conducted as 180.0°C → 127.0°C → 45.0°C. The isothermal crystallization time at 127.0 °C was controlled as 0, 5, 10, and 15 min where the PLLA spherulite grew. After that, the specimen was quenched to 45.0 °C and kept at this temperature for 40 min to induce the crystallization of PEG, as shown in **Figure 26**.

As can be seen from the POM micrographs in **Figure 27(a)**, PEG does not crystallize at 45.0 °C upon the direct quench from melt at 180.0 °C, however at 41°C PEG crystallization was clearly observed. This is due to the freezing temperature ( $T_f$ ) depression of PEG in the mixture of the PLLA/PEG (50/50) blend specimen by noting that  $T_f$  for the neat PEG specimen is 52.0 °C. It should be noted that here we prefer to use the terminology “freezing temperature” instead of “crystallization temperature” to avoid any confusion with the “isothermal crystallization temperature” at which the isothermal crystallization experiment was conducted. Furthermore, the  $T_g$  of the PLLA/PEG (50/50) blend is approximately estimated as  $-8.2$  °C by using the Fox equation with  $T_{g,PEG} = -53.0$  °C [41] and  $T_{g,PLLA} = 59.6$  °C [8]. Therefore, the homogeneous mixture of PLLA and PEG is in the rubbery state at 41°C. However, PLLA crystallization was not observed at 41°C which may be due to the worse crystallizability of PLLA as compared to that of PEG.

The direct evidence of the confined crystallization of PEG inside the preformed PLLA spherulite was observed by the bright-field optical microscopic observation

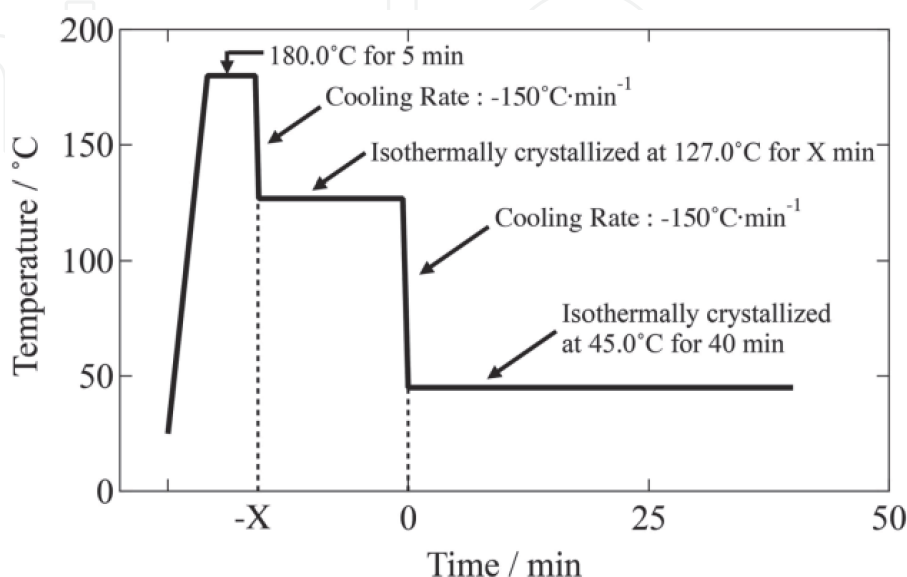


**Figure 26.**

*Temperature protocol for the POM observations and the DSC measurements for the PLLA/PEG (50/50) blend specimens isothermally crystallized by the two-step T-jump (adapted from reference [13] with a permission).*

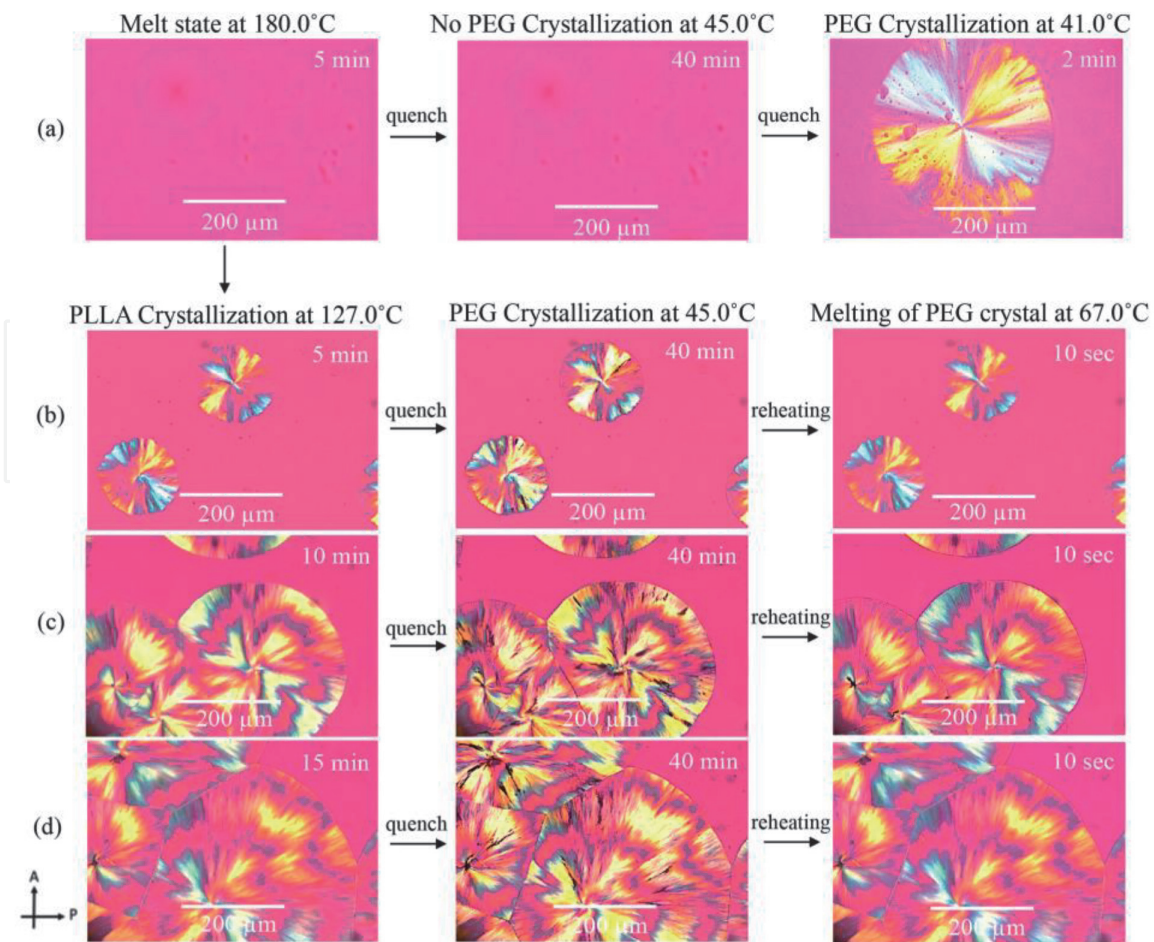


**Figure 27.** POM micrographs showing the crystallization processes of PLLA/PEG (50/50) blend specimens at 45.0 °C (40 min) after the temperature jump from 127.0 °C, where PLLA was allowed to crystallize for (a) 0, (b) 5, (c) 10, and (d) 15 min. Subsequently, the specimens were subjected to reheating with 50°C min<sup>-1</sup> up to 67.0°C. POM images shown in the right column were taken after 10 s of the temperature equilibration at 67.0°C (adapted from reference [13] with a permission).

which is shown in **Figure 28**. Actually, polarizer and analyzer plates were removed after first-step of T-jump at 127.0°C for 600 s. Afterwards, the specimen was quenched to 45.0°C. Around 484–486 s elapsed at 45.0°C, the dark spokes were observed inside the PLLA spherulite which were disappeared when temperature was increased up to 67.0°C. Thus, the confined crystallization of PEG in the preformed PLLA spherulite was evident. Upon further quenching from 67.0°C to 45.0°C, the confined crystallization of PEG again occurred inside the PLLA spherulite, as shown in the bottom row of **Figure 28**. It is interesting to observe that the crystallization of PEG did not start from the center of the preformed PLLA spherulite. It rather seems that the initiation of the PEG crystallization was at random. Also, interesting to note no memory effect, i.e., the trajectories of the second-time PEG crystallization were completely different from the first-time ones. Furthermore, there observed a bridging PEG crystalline region which continuously strides over two-neighboring PLLA spherulites being contacted to each other with a straight boundary.

**Figure 29(a)** shows the change in the WAXS profiles during the isothermal crystallization at 45.0°C after the PLLA crystallization for 15 min at 127.0°C. Initially at  $t = 315$  s, only the PLLA crystalline reflection peaks at  $q = 11.95, 13.43,$  and  $15.45 \text{ nm}^{-1}$  were observed. As time goes on, the PEG crystalline reflection peaks also appear at  $q = 13.56, 15.94, 16.12, 16.30 \text{ nm}^{-1}$  with increasing their intensity. **Figure 29(b)** shows the plots of peak area as a function of time. The peak area for

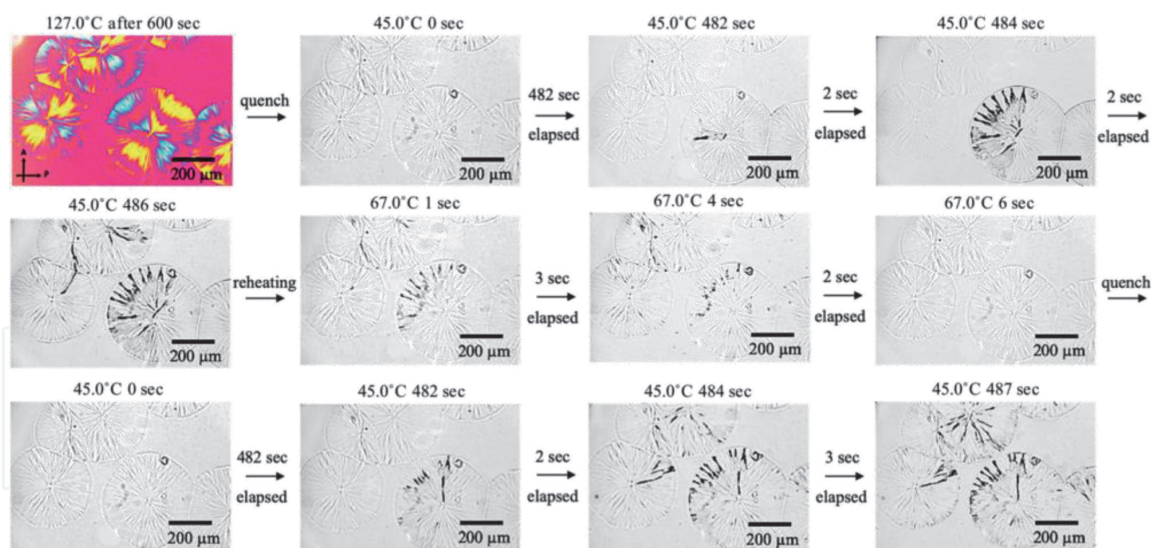


**Figure 28.**

POM image obtained at 127.0°C (600 s isothermal crystallization; shown at the top-left corner) and bright-field micrographs showing the confined crystallization of PEG in the PLLA spherulites for the PLLA/PEG (50/50) blend specimen. The specimen was quickly cooled from the melt state (180.0°C) to the crystallization state of PLLA at 127.0°C. After 600 s elapsed (isothermal crystallization for 600 s at 127.0°C), the specimen was again quenched to 45.0°C for the isothermal crystallization of PEG. Then, the specimen was subjected to reheating up to 67.0°C to melt the PEG crystalline phase. Subsequently (after 6 s elapsed), the specimen was quenched to 45.0°C for the isothermal crystallization at 45.0°C for the second time by keeping the same PLLA spherulites in which the confined crystallization of PEG took place again (adapted from reference [13] with a permission).

the PLLA crystalline peak was unchanged with the time however, that of PEG peaks showed the increasing tendency and then leveled off. The onset time of the peak evolution can be considered as the induction period which was about 5 min for this particular case. Although the peak positions of the PEG reflections in the second-step of T-jump of the blend specimen are the same as those for the neat PEG [13], it is specific to recognize the tremendous suppression of the  $(12\bar{4})/(\bar{1}24)$  reflection peak for the blend specimen as compared to that for the neat PEG [13]. This may indicate the effect of the space confinement that the direction of the PEG crystal growth was suppressed, which is the  $[12\bar{4}]/[\bar{1}24]$  direction almost parallel to the  $c$ -axis, in turn, the polymer chain direction. On the other hand, the  $(120)$  reflection peak was not suppressed, indicating that the PEG crystal growth in the direction perpendicular to the polymer chains was not affected. Assuming the folded-chain crystal of the PEG crystalline lamella, these results suggest the suppression of the lamellar thickening due to the space confinement in the amorphous phase sandwiched by the preformed PLLA crystalline lamellae. This further suggests the orientation of the PEG lamellae parallel to those of PLLA. The parallel orientation of the PEG lamellae (parallel to the preformed PLLA crystalline lamellae) as a consequence of the space confinement can be explained by the previous work of Huang et al. [42].

Such a space confinement effect results in the formation of extraordinarily thin PEG lamellae, in turn the lowering of the melting temperature according to the Gibbs–Thomson equation. To check this speculation, the DSC measurements were conducted. The specimens were first quenched from 180.0°C to 127.0°C to allow isothermal crystallization of PLLA for X min ( $X = 5, 10, 15,$  and  $20$ ) in prior to the second-step T-jump to 45.0°C to allow isothermal PEG crystallization at 45.0°C for 30 min. After the isothermal PEG crystallization at 45.0°C for 30 min, the specimen was then heated with the rate of 10°C/min where the DSC measurement was conducted. **Figure 30** shows the change in  $T_m$  of PEG as a function of the PLLA crystallization time at 127.0°C. It is clear that the  $T_m$ 's of PEG in PLLA/PEG(50/50) blend are much lower than that for the neat PEG crystallized, suggesting the

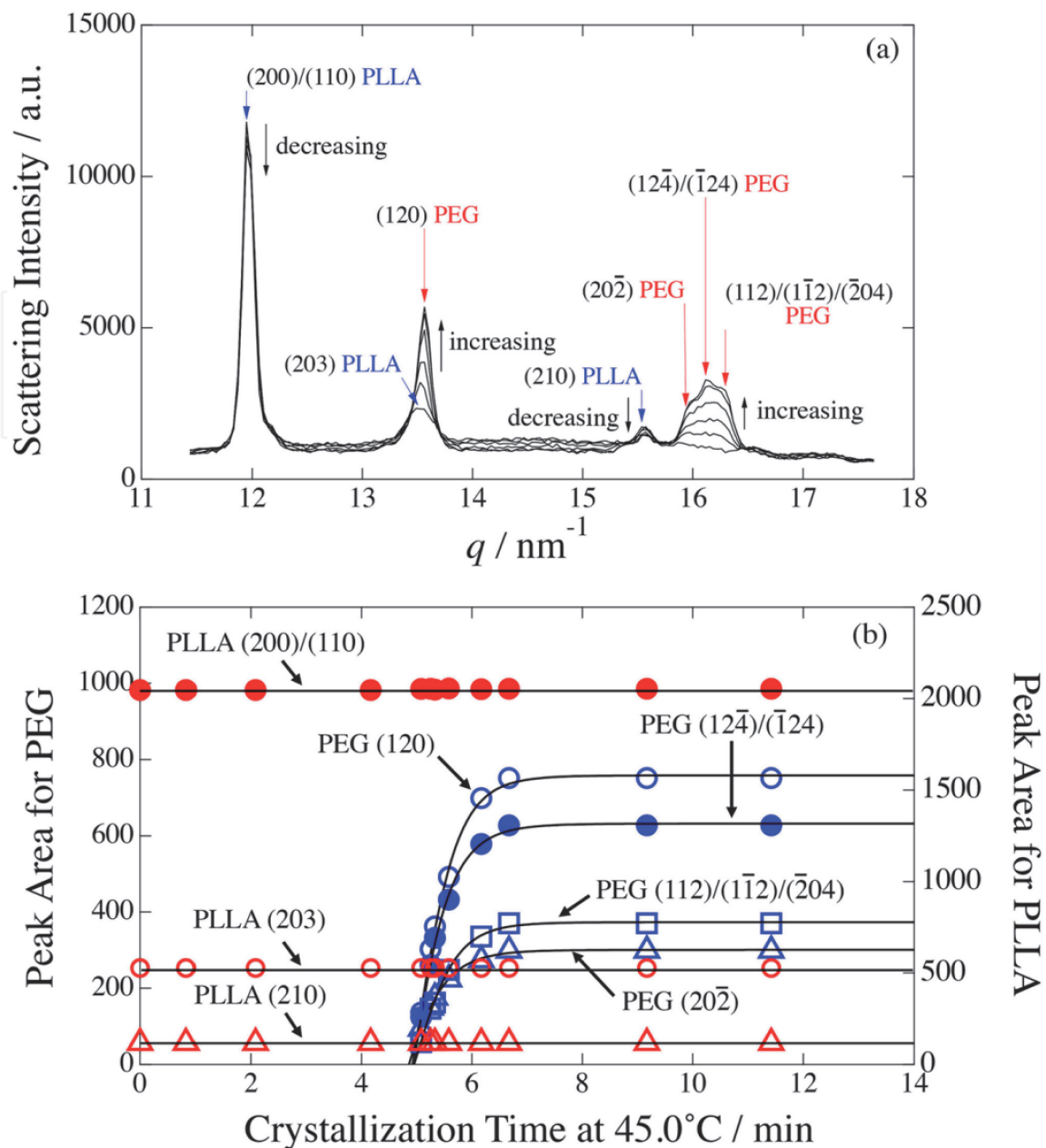


**Figure 29.**  
 (a) Time-resolved 1d-WAXS profiles along the PEG crystallization at 45.0°C in the PLLA/PEG (50/50) blend specimen after PLLA crystallized at 127.0°C for 15 min. (b) Plots of the area of crystallization peaks as a function of time, which was evaluated from WAXS results shown in Figure 29(a) after the peak decomposition (adapted from reference [13] with a permission).

formation of thinner PEG lamellae in case of the confined crystallization. It is noteworthy to observe that  $T_m$  of PEG is monotonically increased with an increase of the PLLA crystallization time, which might imply that the space confinement effect becomes lesser with the growth of the PLLA spherulite and eventually reaching no space confinement effect for the PLLA crystallization time larger than 20 min. Although this tendency seems to be reasonable, it should be noted that thickening of the PLLA lamellae with an increase in the PLLA crystallization time results in more significant confinement to the PEG crystallization taking place in the amorphous region sandwiched by two PLLA crystalline lamellae. Therefore, the result shown in Figure 30 rather implies the effect of the increase in the weight fraction of PEG ( $w_{\text{PEG}}$ ) in the amorphous region comprising the homogeneous mixture of PEG and PLLA. Furthermore, there might be still a weaker confinement, as the density of crystalline PLLA (1.29 g/cm<sup>3</sup>) [43] is higher compared to that of amorphous PLLA (1.25 g/cm<sup>3</sup>) [43]. Consequently, at the same time as PLLA

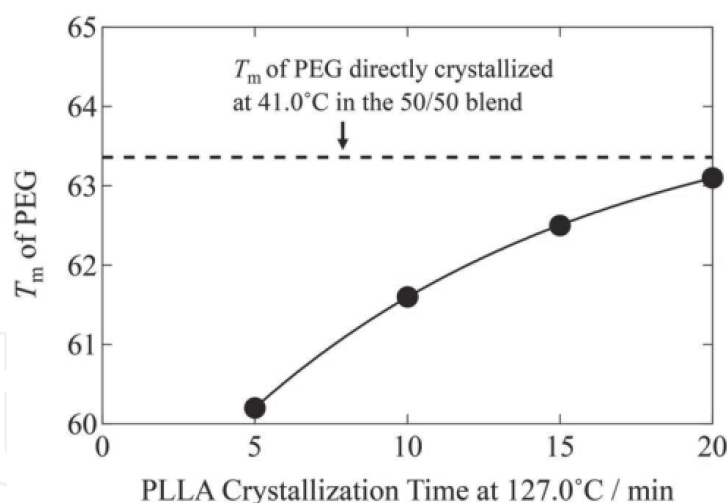


**Figure 30.**

$T_m$  of PEG as a function of the PLLA crystallization time at 127.0°C (adapted from reference [13] with a permission).

lamellae grow in size, the amorphous phase will deplete in PLLA and due to the difference in densities there might be an overall gain in space, which enhances the growth of the PEG lamellae. As this effect becomes larger with the progress in the PLLA crystallization, the PEG lamellae can grow more so that the  $T_m$  of PEG increases with an increase in the PLLA crystallization time at 127°C, as shown in **Figure 30**. Thus, the DSC confirmation of the above-mentioned speculation of the formation of the PEG lamellae oriented parallel to the preformed PLLA lamellae is not satisfactory. We will report results of detailed DSC experiments using several PEG/PLLA blend specimens with different  $w_{\text{PEG}}$  in our future publication.

Furthermore, the  $T_f$  of PEG in the melt mixture of PEG and PLLA amorphous phase were determined by conducting the DSC measurements. Here, it is important to avoid crystallization of PLLA. Therefore, the specimens were quickly cooled from 180°C to 80.0°C and then cooled to 10°C with cooling rate 1, 2.5 and 10°C/min. We conducted cooling-rate dependencies to correct for the cooling-rate effect on this temperature and to evaluate  $T_f$  of PEG by the extrapolation of the onset temperature of the exothermic peak to the zero-cooling rate [13]. Thus-evaluated  $T_f$  of PEG is plotted as a function of  $w_{\text{PEG}}$  for the PLLA/PEG blend specimens in **Figure 31(a)**. It can be seen that  $T_f$  is increased when  $w_{\text{PEG}}$  is increased. Based on this plot, the mechanism of the confined crystallization in the preformed PLLA spherulites is considered. Upon the crystallization of PLLA from the melt of the PLLA/PEG amorphous phase, the PEG content in the amorphous region inside the PLLA spherulite is increased so that  $T_f$  is increased from its original one ( $T_f = 45.3^\circ\text{C}$ ) at  $w_{\text{PEG}} = 0.5$ . The fact that no PEG crystallization at 45.0°C (**Figure 27(a)**) was observed for this blend specimen with  $w_{\text{PEG}} = 0.5$  seems to conflict with the fact of  $T_f = 45.3^\circ\text{C}$ . Since this value ( $T_f = 45.3^\circ\text{C}$ ) was estimated by the extrapolation of the onset temperature of the PEG crystallization to the zero-cooling rate, the PEG crystallization at 45.0°C would take infinitely long time for this blend specimen (PLLA/PEG (50/50)). **Figure 27(a)** showing no PEG crystallization at 45.0°C implies that the PEG crystallization would take place more than 40 min. Consequently, it can be considered that when the PLLA crystallization time at 127.0°C is longer, the PEG content in the amorphous region becomes higher so that the PEG crystallizability becomes more sufficient. The experimental results definitely supported this speculation.

Next, the PEG fraction in the amorphous phase in the preformed PLLA spherulite was estimated by DSC measurements. The PLLA/PEG (50/50) blend specimens

were annealed at 180.0°C for 5 min, and then quenched first to 127.0°C for 10 min to form the PLLA spherulites. Afterward, the specimens were quenched to 60.0°C and then cooled gradually down to room temperature and DSC scans were observed [13]. Thus-evaluated  $T_f$  of PEG are plotted as a function of the crystallization time of PLLA at 127.0°C in **Figure 31(b)**. Based on the result shown in **Figure 31(b)** combined with **Figure 31(a)** it was possible to estimate  $w_{\text{PEG}}$ , which is increased from  $w_{\text{PEG}} = 0.5$  with increasing of PLLA crystallization time at 127.0°C. **Figure 32** shows the  $\Delta w_{\text{PEG}} (= w_{\text{PEG}} - 0.5)$  behavior as a function of the PLLA crystallization time. It is clearly observed that  $w_{\text{PEG}}$  is increased with increasing of PLLA crystallization time at 127.0°C, which supports the above-mentioned discussion that  $w_{\text{PEG}}$  in the amorphous region inside the larger PLLA spherulite is larger than that inside the

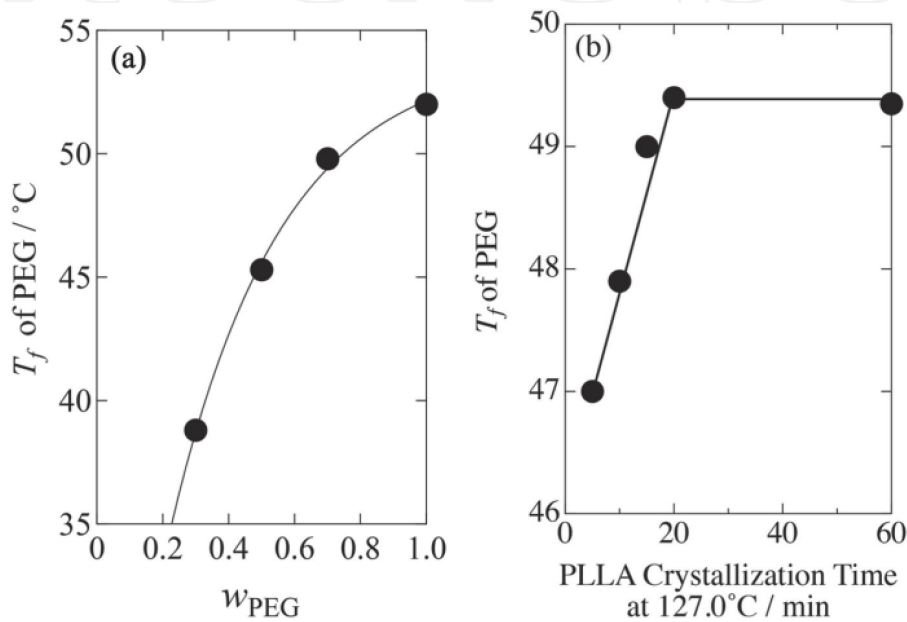


**Figure 31.** (a) Dependence of the freezing temperature of PEG ( $T_f$ ) on the weight fraction of PEG ( $w_{\text{PEG}}$ ) in the PLLA/PEG blend specimens. (b) Dependence of  $T_f$  of PEG on the PLLA crystallization time at 127.0°C (adapted from reference [13] with a permission).

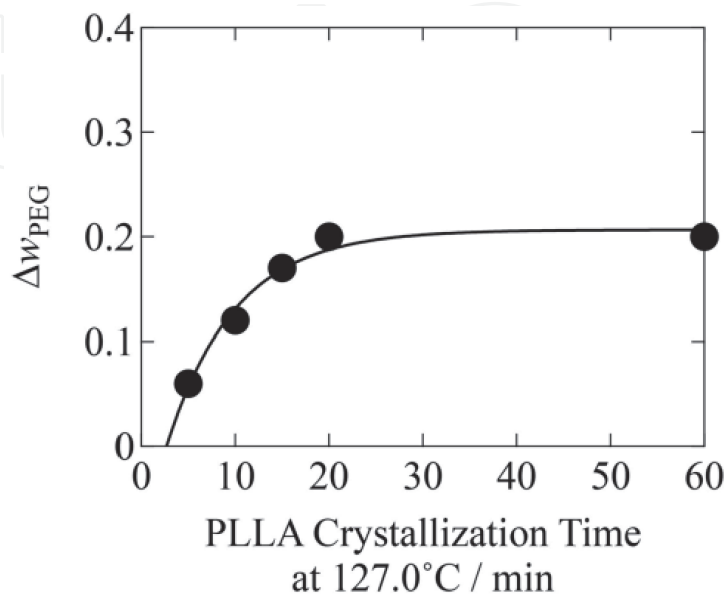


**Figure 32.** Plot of  $w_{\text{PEG}}$  as a function of the PLLA crystallization time at 127.0°C (adapted from reference [13] with a permission).

smaller PLLA spherulite because of the progress in the PLLA crystallization. It is noteworthy that it leveled off around 20 min, suggesting completeness of the PLLA crystallization at 127.0°C around 20 min.

## 5. Confined crystallization of PCL in the block copolymer of PLA and PCL

In this section, we focus on block copolymers of PLA with PCL, namely, PLLA-PCL diblock copolymers and PLLA-PCL-PDLA triblock copolymers with respect to the confined crystallization within the microphase-separated domain of PCL which is sandwiched by the glassy PLLA microphase. In this study, PLLA, PDLA, PCL and their block copolymers were synthesized. The polymer synthesis method is described in Ref. [12]. The molecular weight information is reported in **Table 2**. The diblock copolymers are represented by XCL-YL and XCL-YD where X and Y denote the block length or the number-average molecular weights ( $M_n$ ) in kDa of the component PCL (CL), PLLA (L), and PDLA (D) blocks. Whereas, the tri-stereoblock (trisp) copolymers are represented by XCL-YL-ZD where X, Y, and Z denote the block lengths or  $M_n$  values in kDa of its following block sequences shown by the abbreviated symbols. Further, the synthesized diblock copolymers were blended with their corresponding enantiomers, which are abbreviated as B\_X-Y where X and Y denote the block length. For example, B\_10-10 shows the blend of 10CL-10 L and 10CL-10D. Furthermore, all the prepared specimens were hot-pressed followed by quenching in ice-water, to obtain polymer films.

The DSC thermograms of the block copolymers compared with that of neat PCL and neat PDLA are shown in **Figure 33**. The enthalpy of melting ( $\Delta H_m$ ) of PCL decreases from 42.4 to 20.2 J/g with increasing the block length of PDLA, whereas the  $\Delta H_m$  of PDLA is increased from 36.8 to 43.4 J/g. These changes in enthalpy correspond to the decreasing content of PCL and increasing content of PDLA in the copolymer system. Furthermore, different melting peaks of PCL and PDLA confirms separate crystallization of PCL and PDLA blocks of varying length. **Figure 33(b)** shows the DSC results of the enantiomeric diblock copolymer blends and the trisp copolymer in the heating scan (10°C/min). As can be seen in the figure, the specimen B\_10-10 form perfect SC crystal upon blending, without generating the HC. This is because of the low molecular weight of the PDLA/PLLA blocks. Furthermore, double melting peaks were observed for SC crystal at 221.8°C and 235.4°C which may be due to the formation of relatively thinner and thicker lamellae of SC crystal. It should be noted that more formation of HC in B\_10-20 and B\_10\_30 specimen is due to the increasing molecular weight of PLLA/PDLA blocks. Therefore, it can be concluded that the higher molecular weight of the block sequences increases the formation of HC instead of SC.

Specimen	$M_n$	$M_w$	$M_w / M_n$
10CL-10D	48.6	71.8	1.47
10CL-10 L	45.5	69.8	1.53
10CL-10 L-10D	59.0	100.6	1.70
10CL-20D	64.0	107.2	1.67
10CL-30D	69.8	160.5	2.30

**Table 2.**  
Molecular weight of the synthesized block copolymers (analyzed by GPC).

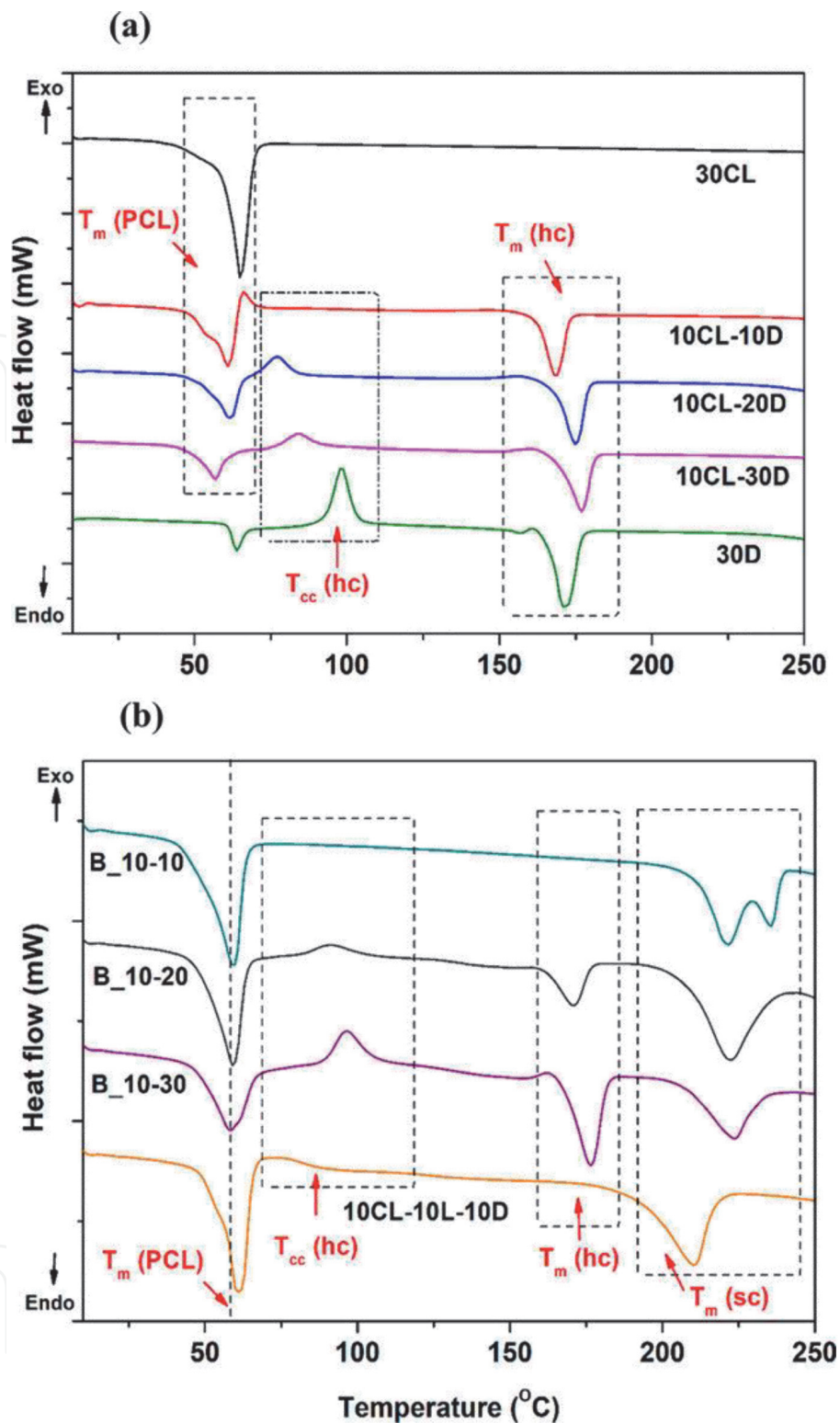


**Figure 33.** DSC thermograms of (a) neat PCL, neat PDLA, and PCL-PDLA diblock copolymers and (b) enantiomeric diblock copolymer blends and trisb copolymer (adapted from reference [12] with a permission).

The stress-strain (SS) curves of the polymer films of the block copolymers and their enantiomeric blends as well as that of the trisb copolymer are shown in **Figure 34**. As can be seen that the elongation of 30PCL specimen is higher than that of 30D specimen. The higher elongation of PCL is due to its soft and flexible nature as the stress-strain test is performed at 25°C (rubbery region of PCL) while PDLA is in glassy state. The tensile strength, modulus, and the toughness of the diblock copolymers are enhanced with increasing the block length of PDLA. The highest elongation at break was found for the specimen 10CL-30D. To understand such an



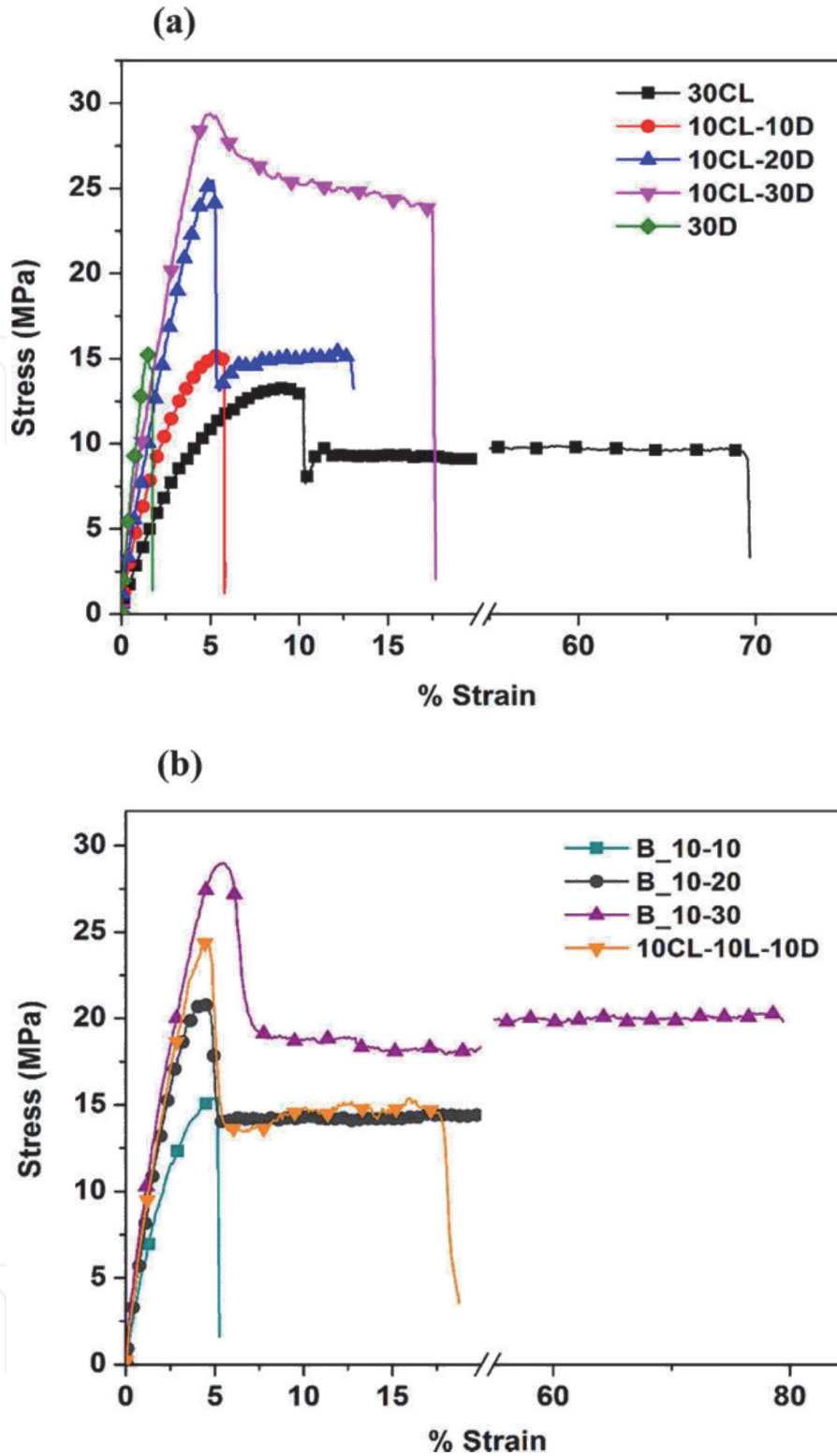


**Figure 34.**

Representative data for stress vs. (%) Strain of (a) homopolymers and diblock copolymers; (b) diblock blends and triblock copolymer (adapted from reference [12] with a permission).

unusual increase in elongation at break for 10CL-30D, it is important to consider the structure at the amorphous state at higher temperature. Here, it is noted that PCL/PLLA polymer blends exhibit LCST (lower critical solution temperature) phase behavior [44] so that PCL-PLLA blends are subjected to microphase separation at higher temperature. As a matter of fact, the SAXS results (Figure 35) indicated the microphase separation at higher temperature (210°C) for the PCL-PDLA diblock copolymers. The judgment of morphology was uncertain due to the presence of only a first order peak. For the 10CL-30D specimen, there may be the

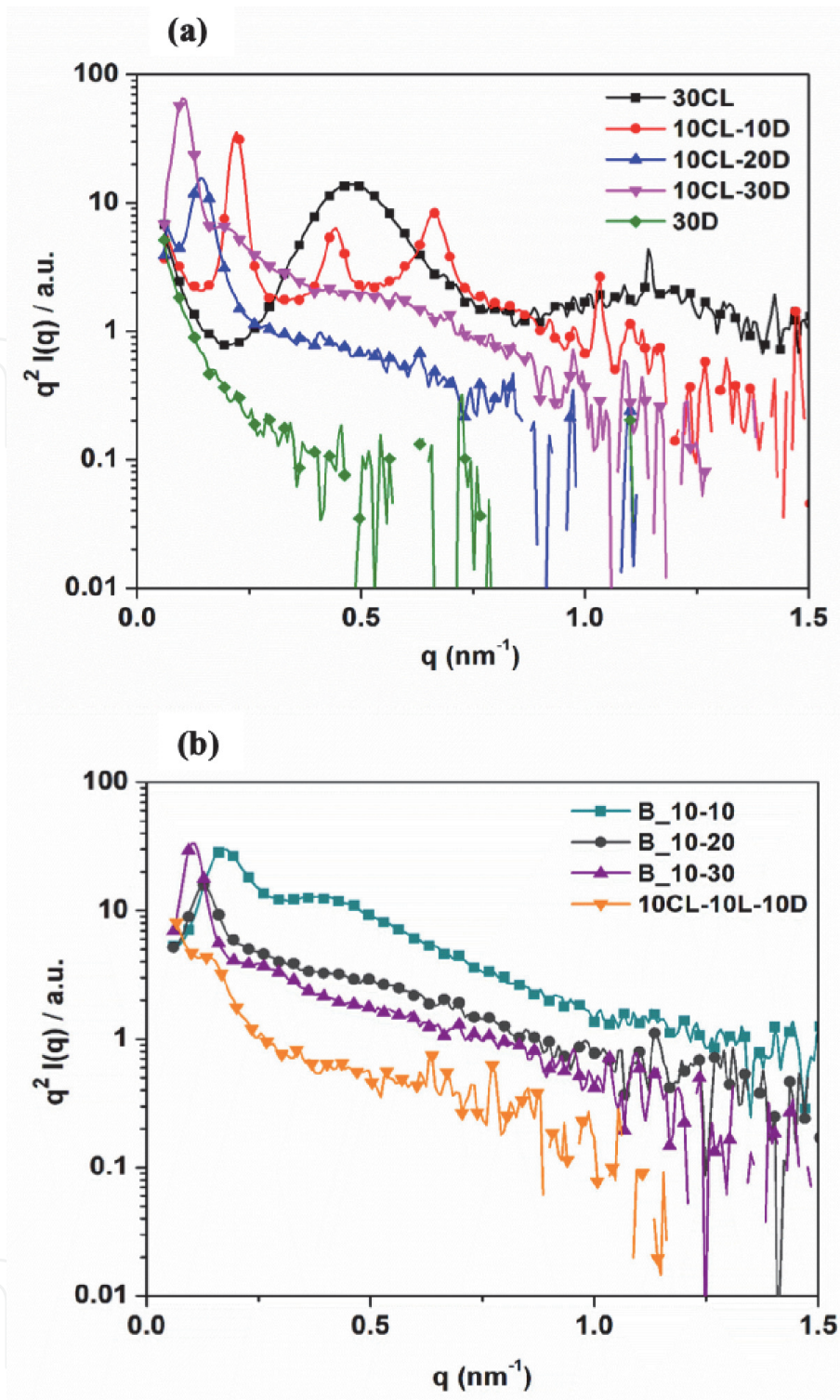


**Figure 35.** Lorentz-corrected scattering intensity vs.  $q$  of (a) homopolymers and diblock copolymers and (b) enantiomeric diblock copolymer blends and triblock copolymer (adapted from reference [12] with a permission).

possibility of the formation of PCL lamellar or cylindrical microdomains due to the PCL fraction being 25%. It may be perceived that upon rapid quenching from 210 to 0°C, the PDLA matrix is vitrified due to which the PCL block chains would only crystallize in the interior of the cylindrical microdomains surrounded by the glassy matrix. Because of the confined crystallization, the crystallite may be considered as tiny and dispersed in the interior of PCL microdomains. In such a situation, the crack propagation of glassy PDLA matrix is terminated at the PCL microdomains when the specimen is drawn which could be attributed to amorphous PCL phase (rubbery domain) at room temperature. Also, the PCL block chains are much easier

to be unfolded from the tiny crystalline lamellae as compared to larger (thicker) lamellae in other specimens. Therefore, the 10CL-30D specimen is found to exhibit the most stretchable character which may be ascribed to its structural origin.

## 6. Conclusions

The crystallization of PLLA is one of the key factor for analyzing structure–property relationships of PLLA-based blend, block copolymer and nanocomposites. The presence of solid state additives (SFN and CNC) increased the nucleation of PLLA, thus influences the whole crystallization process, however the spherulite growth of PLLA was not significantly changed by loading SFN or CNC. For the case of liquid-state additive i.e. OMG, nucleation and spherulite growth rate both were found to be increased which improves the crystallizability of PLLA. The presence of SFN enhanced the SC crystallization while it suppressed the HC crystallization. It is noteworthy for this particular case that the spherulite growth rate was suppressed by the addition of 1% SFN whereas the nucleation density was much increased by SFN. For the case of PLLA/PEG(50/50) blend, a two-step temperature-jump was conducted as  $180.0^{\circ}\text{C} \rightarrow 127.0^{\circ}\text{C} \rightarrow 45.0^{\circ}\text{C}$ . For this particular condition, it was found that PEG can crystallize only in the preformed spherulites of PLLA. The confined crystallization of PEG can be accounted for as follows. Upon the PLLA crystallization at  $127.0^{\circ}\text{C}$ , the PEG content in the amorphous region inside the PLLA spherulite is increased because of the formation of the pure solid phase of PLLA (crystalline phase). Then,  $T_f$  of PEG increases so that PEG can crystallize but this crystallization is only allowed inside the PLLA spherulite. The direct evidence of the PEG crystallization was obtained by the bright-field optical microscopic observation and WAXS measurements. For the case of PLA and PCL block copolymers, the poor mechanical property of PDLA (which is poor elongation at break) was reported to be much improved by the presence of extensible PCL block component even in case of a short PCL chain in the block copolymer, which may be ascribed to the confined crystallization of PCL in the microdomain structure. Furthermore, the formation of SC crystal in the enantiomeric blend of PLLA-*b*-PCL and PDLA-*b*-PCL have been examined by changing the block length of PLLA and PDLA components.

### Author details


Amit Kumar Pandey<sup>1</sup> and Shinichi Sakurai<sup>1,2\*</sup>

<sup>1</sup> Department of Biobased Materials Science, Kyoto Institute of Technology, Japan

<sup>2</sup> Indian Institute of Technology Guwahati, India

\*Address all correspondence to: shin@kit.ac.jp

### IntechOpen

© 2021 The Author(s). Licensee IntechOpen. This chapter is distributed under the terms of the Creative Commons Attribution License (<http://creativecommons.org/licenses/by/3.0>), which permits unrestricted use, distribution, and reproduction in any medium, provided the original work is properly cited. 

## References

- [1] Saeidlou, S.; Huneault, M.A.; Li, H.; Park, C.B. Poly(lactic acid) crystallization. *Prog. Polym. Sci.* **2012**, *37*, 1657–1677.
- [2] Wasanasuk, K.; Tashiro, K.; Hanesaka, M.; Ohhara, T.; Kurihara, K.; Kuroki, R.; Tamada, T.; Ozeki, T.; Kanamoto, T. Crystal structure analysis of poly(l-lactic acid)  $\alpha$  form on the basis of the 2-dimensional wide-angle synchrotron X-ray and neutron diffraction measurements. *Macromolecules* **2011**, *44*, 6441–6452.
- [3] Wasanasuk, K.; Tashiro, K. Structural regularization in the crystallization process from the glass or melt of poly(l-lactic acid) viewed from the temperature-dependent and time-resolved measurements of FTIR and wide-angle/small-angle X-ray scatterings. *Macromolecules* **2011**, *44*, 9650–9660.
- [4] Zhang, J.; Tashiro, K.; Tsuji, H.; Domb, A.J. Disorder-to-order phase transition and multiple melting behavior of poly(L-lactide) investigated by simultaneous measurements of WAXD and DSC. *Macromolecules* **2008**, *41*, 1352–1357.
- [5] Zhang, J.; Tashiro, K.; Domb, A.J.; Tsuji, H. Confirmation of disorder  $\alpha$  form of poly(L-lactic acid) by the X-ray fiber pattern and polarized IR/Raman spectra measured for uniaxially-oriented samples. *Macromol. Symp.* **2006**, *242*, 274–278.
- [6] Aleman, C.; Lotz, B.; Puiggali, J. Crystal Structure of the  $\alpha$ -Form of Poly (L-lactide). *Macromolecules* **2001**, *34*, 4795–4801.
- [7] Thi Ngoc Diep, P.; Mochizuki, M.; Doi, M.; Takagi, H.; Shimizu, N.; Igarashi, N.; Sasaki, S.; Sakurai, S. Effects of a special diluent as an agent of improving the crystallizability of poly (L-lactic acid). *Polym. J.* **2019**, *51*, 283–294.
- [8] Pandey, A.K.; Katiyar, V.; Sasaki, S.; Sakurai, S. Accelerated crystallization of poly(l-lactic acid) by silk fibroin nanodisc. *Polym. J.* **2019**.
- [9] Pandey, A.K.; Katiyar, V.; Takagi, H.; Shimizu, N.; Igarashi, N.; Sasaki, S.; Sakurai, S. Structural Evolution in Isothermal Crystallization Process of Poly(L-lactic acid) Enhanced by Silk Fibroin Nano-Disc. *Materials.* **2019**, *12*, 1872.
- [10] Thi Ngoc Diep, P.; Takagi, H.; Shimizu, N.; Igarashi, N.; Sasaki, S.; Sakurai, S. Effects of Loading Amount of Plasticizers on Improved Crystallization of Poly (L-lactic acid). *J. Fiber Sci. Technol.* **2019**, *75*, 99–111.
- [11] Pandey, A.K.; Diep, P.T.N.; Patwa, R.; Katiyar, V.; Sasaki, S.; Sakurai, S. DSC and SWAXS Studies on the Effects of Silk Nanocrystals on Crystallization of Poly(l-Lactic Acid). In *Advances in Sustainable Polymers*; Springer, **2020**; pp. 321–339.
- [12] Mulchandani, N.; Gupta, A.; Masutani, K.; Kumar, S.; Sakurai, S.; Kimura, Y.; Katiyar, V. Effect of Block Length and Stereocomplexation on the Thermally Processable Poly ( $\epsilon$ -caprolactone) and Poly (Lactic acid) Block Copolymers for Biomedical Applications. *ACS Appl. Polym. Mater.* **2019**, *1*, 3354–3365.
- [13] BANPEAN, A.; SAKURAI, S. Confined Crystallization of Poly (ethylene glycol) in Spherulites of Poly (L-lactic acid) in a PLLA/PEG Blend. *Polymer.* **2021**, 123370.
- [14] Mondal, K.; Sakurai, S.; Okahisa, Y.; Goud, V. V.; Katiyar, V. Effect of cellulose nanocrystals derived from *Dunaliella tertiolecta* marine green algae

residue on crystallization behaviour of poly(lactic acid). Submitted to *Carbohydr. Polym.* **2020**.

[15] Pandey, A.K.; Takagi, H.; Igarashi, N.; Shimizu, N.; Sakurai, S. Exclusive Formation of Stereocomplex Crystallites in Poly(L-lactic acid)/Poly(D-lactic acid) Blends Promoted by Silk Fibroin Nanodisc. Submitted to *Macromolecules* **2021**.

[16] Li, H.; Huneault, M.A. Effect of nucleation and plasticization on the crystallization of poly (lactic acid). *Polymer.* **2007**, *48*, 6855–6866.

[17] Carbone, M.J.; Vanhalle, M.; Goderis, B.; Puyvelde, P. Van Amino acids and poly ( amino acids ) as nucleating agents for poly ( lactic acid ). **2015**, *35*, 169–180.

[18] Kawamoto, N.; Sakai, A.; Horikoshi, T.; Urushihara, T.; Tobita, E. Nucleating agent for poly(L-lactic acid) - An optimization of chemical structure of hydrazide compound for advanced nucleation ability. *J. Appl. Polym. Sci.* **2007**, *103*, 198–203.

[19] Ouchiar, S.; Stoclet, G.; Cabaret, C.; Gloaguen, V. Influence of the Filler Nature on the Crystalline Structure of Polylactide-Based Nanocomposites: New Insights into the Nucleating Effect. *Macromolecules* **2016**, *49*, 2782–2790.

[20] Müller, A.J.; Ávila, M.; Saenz, G.; Salazar, J. *CHAPTER 3. Crystallization of PLA-based Materials*; 2015; ISBN 9781782624806.

[21] Patwa, R.; Soundararajan, N.; Mulchandani, N.; Bhasney, S.M.; Shah, M.; Kumar, S.; Kumar, A.; Katiyar, V. Silk nano-discs: A natural material for cancer therapy. *Biopolymers* **2018**, *109*, 23231.

[22] Tsuji, H. Poly(lactic acid) stereocomplexes: A decade of progress. *Adv. Drug Deliv. Rev.* **2016**, *107*, 97–135.

[23] Tan, B.H.; Muiruri, J.K.; Li, Z.; He, C. Recent Progress in Using Stereocomplexation for Enhancement of Thermal and Mechanical Property of Polylactide. *ACS Sustain. Chem. Eng.* **2016**, *4*, 5370–5391.

[24] Tsuji, H.; Ikada, Y. Stereocomplex Formation between Enantiomeric Poly (lactic acid)s. 9. Stereocomplexation from the Melt. *Macromolecules* **1993**, *26*, 6918–6926.

[25] Okihara, T.; Tsuji, M.; Kawaguchi, A.; Katayama, K.I.; Tsuji, H.; Hyon, S. H.; Ikada, Y. Crystal Structure of Stereocomplex of Poly(L-lactide) and Poly(D-lactide). *J. Macromol. Sci. Part B* **1991**, *30*, 119–140.

[26] Tsuji, H.; Fukui, I. Enhanced thermal stability of poly(lactide)s in the melt by enantiomeric polymer blending. *Polymer.* **2003**, *44*, 2891–2896.

[27] Long, H.; Wu, Z.; Dong, Q.; Shen, Y.; Zhou, W.; Luo, Y.; Zhang, C.; Dong, X. Effect of polyethylene glycol on mechanical properties of bamboo fiber-reinforced polylactic acid composites. *J. Appl. Polym. Sci.* **2019**, *136*, 47709.

[28] Liu, H.; Zhang, J. Research progress in toughening modification of poly (lactic acid). *J. Polym. Sci. part B Polym. Phys.* **2011**, *49*, 1051–1083.

[29] Lai, W.-C.; Liao, W.-B.; Lin, T.-T. The effect of end groups of PEG on the crystallization behaviors of binary crystalline polymer blends PEG/PLLA. *Polymer.* **2004**, *45*, 3073–3080.

[30] Li, Y.; Li, X.; Xiang, F.; Huang, T.; Wang, Y.; Wu, J.; Zhou, Z. Crystallization, rheological, and mechanical properties of PLLA/PEG blend with multiwalled carbon nanotubes. *Polym. Adv. Technol.* **2011**, *22*, 1959–1970.

[31] Kulinski, bZ; Piorkowska, E. Crystallization, structure and properties

- of plasticized poly (L-lactide). *Polymer*. **2005**, *46*, 10290–10300.
- [32] Piorkowska, E.; Kulinski, Z.; Galeski, A.; Masirek, R. Plasticization of semicrystalline poly (L-lactide) with poly (propylene glycol). *Polymer*. **2006**, *47*, 7178–7188.
- [33] Zhao, X.; Hu, H.; Wang, X.; Yu, X.; Zhou, W.; Peng, S. Super tough poly (lactic acid) blends: a comprehensive review. *RSC Adv*. **2020**, *10*, 13316–13368.
- [34] Tsuji, H.; Ikada, Y. Properties and morphologies of poly (L-lactide): 1. Annealing condition effects on properties and morphologies of poly (L-lactide). *Polymer*. **1995**, *36*, 2709–2716.
- [35] Strobl, G.R.; Strobl, G.R. *The physics of polymers*; Springer, 1997; Vol. 2;.
- [36] Padden Jr, F.J.; Keith, H.D. Mechanism for lamellar branching in isotactic polypropylene. *J. Appl. Phys*. **1973**, *44*, 1217–1223.
- [37] Yamada, K.; Matsumoto, S.; Tagashira, K.; Hikosaka, M. Isotacticity dependence of spherulitic morphology of isotactic polypropylene. *Polymer*. **1998**, *39*, 5327–5333.
- [38] Uchida, K.; Mita, K.; Higaki, Y.; Kojio, K.; Takahara, A. Lamellar orientation in isotactic polypropylene thin films: a complement study via grazing incidence X-ray diffraction and surface/cross-sectional imaging. *Polym. J*. **2019**, *51*, 183–188.
- [39] Hama, H.; Tashiro, K. Structural changes in isothermal crystallization process of polyoxymethylene investigated by time-resolved FTIR, SAXS and WAXS measurements. *Polymer*. **2003**, *44*, 6973–6988.
- [40] Patterson, A.L. The scherrer formula for X-ray particle size determination. *Phys. Rev*. **1939**, *56*, 978–982.
- [41] Faucher, J.A.; Koleske, J. V; Santee Jr, E.R.; Stratta, J.J.; Wilson Iii, C.W. Glass transitions of ethylene oxide polymers. *J. Appl. Phys*. **1966**, *37*, 3962–3964.
- [42] Huang, P.; Zhu, L.; Guo, Y.; Ge, Q.; Jing, A.J.; Chen, W.Y.; Quirk, R.P.; Cheng, S.Z.D.; Thomas, E.L.; Lotz, B. Confinement size effect on crystal orientation changes of poly (ethylene oxide) blocks in poly (ethylene oxide)-b-polystyrene diblock copolymers. *Macromolecules* **2004**, *37*, 3689–3698.
- [43] E.W. Fischer, H.J. Sterzel, and G. Wegner, Investigation of the structure of solution grown crystals of lactide copolymers by means of chemical reactions. *Kolloid-Z.Z. Polym*. **1973**, *251(11)*, 980–990.
- [44] Meredith, J.C.; J. Amis, E. LCST phase separation in biodegradable polymer blends: poly (D, L-lactide) and poly ( $\epsilon$ -caprolactone). *Macromol. Chem. Phys*. **2000**, *201*, 733–739.